Submitted to the *Astrophysical Journal*

An In-Depth Study of the Abundance Pattern in the Hot Interstellar Medium in NGC 4649

Michael Loewenstein[1]

Department of Astronomy, University of Maryland, College Park, MD 20742

Michael.Loewenstein.1@nasa.gov

and

David S. Davis[2]

Department of Physics, University of Maryland Baltimore County, Baltimore, MD 21250

David.S.Davis@nasa.gov

ABSTRACT

We present our X-ray imaging spectroscopic analysis of data from deep *Suzaku* and *XMM-Newton* Observatory exposures of the Virgo Cluster elliptical galaxy NGC 4649 (M60), focusing on the abundance pattern in the hot interstellar medium (ISM). All measured elements show a radial decline in abundance, with the possible exception of O. We construct steady state solutions to the chemical evolution equations that include infall in addition to stellar mass return and SNIa enrichment, and consider recently published SNIa yields. By adjusting a single model parameter to obtain a match to the global abundance pattern in NGC 4649 we infer that accretion of subsolar metallicity external gas has reduced the overall ISM metallicity and diluted the effectiveness of SNIa to skew the pattern towards low α/Fe ratios, and estimate the combination of SNIa rate and level of dilution. Evidently, newly-introduced gas is heated as it is integrated into, and interacts with, the hot gas that is already present. These results indicate a complex flow and enrichment history for NGC 4649, reflecting the continual evolution of

[1]CRESST and X-ray Astrophysics Laboratory, NASA/GSFC, Greenbelt, MD.

[2]CRESST and Astroparticle Physics Laboratory, NASA/GSFC, Greenbelt, MD.

elliptical galaxies beyond the formation epoch. The heating and circulation of accreted gas may help reconcile this dynamic history with the mostly passive evolution of elliptical stellar populations. In an appendix we examine the effects of the recent updated atomic database *AtomDB* in spectral fitting of thermal plasmas with hot ISM temperatures in the elliptical galaxy range.

Subject headings: galaxies: abundances, galaxies: elliptical and lenticular, galaxies: individual (NGC 4649), galaxies: ISM

1. Introduction

There are two basic approaches to studying the formation and evolution of elliptical galaxies. One may directly examine the assembly history of the baryonic component by observing how the space density and morphological demographics of the population of elliptical galaxies, and their progenitors, develop over time. Alternatively one may conduct detailed investigation of those spectro-photometric properties that reflect their histories, and the scaling relations among these properties. While surveys at a range of redshifts indicate significant growth in both the number and sizes of ellipticals, "archeological" investigation finds that elliptical galaxy stellar populations are mostly in place at high redshifts ($z > 2$ for massive systems) and passively evolve thereafter. Resolution of this apparent paradox is crucial for validation and elucidation of the prevailing hierarchical assembly paradigm of galaxy formation, where dynamical evolution and the triggering of star formation are presumed to be interconnected.

The archeological approach traditionally relies on optical photometry and spectroscopy of the stellar population; however, the hot interstellar medium (ISM) provides a rich complementary site of diagnostic data that is accessible by means of X-ray observation (Loewenstein & Davis 2010, hereafter Paper I, and references therein; Pipino & Mattecucci 2011, hereafter PM11). The physical properties of the ISM in giant elliptical galaxies reflect the distinctive history and nature of these systems and, as such, markedly differ from those in the ISM of spiral galaxies such as the Milky Way. The most striking contrast is that, while mass loss from evolved stars is a primary source of gas in both spirals and ellipticals, most of the mass return in the latter is promptly heated to the high temperatures corresponding to the stellar velocity dispersion and does not currently participate in an ongoing star-gas cycle (Mathews & Brighenti 2003).

This distinct ecology provides a repository of information about processes in the distant and recent past of elliptical galaxies. The ISM is more responsive to energetic events than

the stellar population which is, to first order, passively evolving. Evidence of feedback processes subsequent to the establishment of the stars and the nuclear supermassive black hole (SMBH) can only be found in the ISM. The ISM mass within elliptical galaxies is a small fraction of the stellar mass return integrated over the post-star-formation history of an elliptical galaxy, implying the existence of some steady and/or episodic means of gas removal into the intergalactic, or some circumgalactic, medium. A successful gasdynamical model for ellipticals must explain ISM that generally are, nevertheless, sufficiently massive to rule out persistent supersonic or transonic galactic winds, and also display a large scatter in gas-to-stellar mass ratio ($M_{\rm gas}/M_{\rm stars}$; Mathews et al. 2006 and references therein). While ram pressure stripping may be important at times for some ellipticals in rich clusters, large scale flows driven by Type Ia supernovae (SNIa) and active galactic nuclei (AGN) likely dominate the redistribution of the ISM and its removal from the galaxy.

The amount of energy associated with SNIa exploding at the estimated rate in ellipticals is sufficient to drive a galactic wind. Although effects such as depletion through the formation of dust (PM11) may reduce the discrepancy, the high expected ISM Fe abundance is at odds with X-ray observations (e.g., Paper I, PM11), and a certain amount of fine-tuning in the SNIa rate as a function of time is required for SNIa-driven winds to explain the $M_{\rm gas}/M_{\rm stars}$ scatter without driving out virtually all of the gas and rendering ellipticals undetectable as diffuse soft X-ray sources. Feedback from active galactic nuclei (AGN), implicated in quenching star formation in ellipticals (Schawinski et al. 2007; Cattaneo et al. 2009) and establishing the scaling relations between SMBH mass and stellar mass or velocity dispersion (e.g., DeBuhr, Quataert, & Ma 2011 and references therein), may also drive galactic flows at later times. AGN interaction with hot ISM is evident in *Chandra* X-ray Observatory observations of several ellipticals (McNamara & Nulsen 2007; Nulsen et al. 2009). AGN feedback is fundamentally self-regulating and intermittent: the SMBH is fueled by an initial inflow that is subsequently reversed as the AGN powers up, thus cutting off the supply of gas and enabling the cycle to restart as gas once again flows inward towards the now-dormant SMBH. There has been great progress in implementing and applying hydrodynamical simulations that include various feedback prescriptions (Mathews, Brighenti, & Buote 2004; Brighenti et al. 2009; Ciotti, Ostriker, & Proga 2010), however it remains to be seen whether the full range of ISM observables – X-ray luminosities, temperatures, metallicities and abundance patterns – and their galaxy-to-galaxy variations can be accurately and self-consistently modeled without additional, and perhaps fundamental, adjustment (Mathews & Brighenti 2003). In addition, many ellipticals are embedded in an extended hot intergalactic or circumgalactic medium, and may interact with their environment in a variety of ways (Mulchaey & Jeltema 2010). In particular ellipticals may accrete some combination of primordial gas and gas ejected from winds at earlier epochs (Pipino & Matteucci 2004; Davé et al. 2011). Such an

external medium may also confine outflows.

Recent X-ray measurements of elemental abundances in the hot ISM of ellipticals beg consideration in determining the future direction of these models, and constraining more general theories of the chemical evolution of these systems. The ISM abundance pattern may be a particularly sensitive diagnostic of dynamical processes in ellipticals. If the sole source of interstellar gas is stellar mass loss, the ISM abundance pattern in ellipticals will reflect that in evolved stars found to have $[\alpha/Fe]_{\rm stars} > 0$ ($[\alpha/Fe]_{\rm stars}$ is defined as the log of the abundance ratio, with respect to Fe, of elements primarily produced through α capture to Fe – relative to the solar ratio). Because the internal injection and flow of energy, and the various mechanisms of mass exchange with the external environment, each imprint distinctive departures from the baseline ISM abundance pattern determined by local stellar mass loss, this pattern may be analyzed to probe for signatures of these processes.

Measurement of elliptical galaxy abundance patterns encompassing a broad range of elements, and extending to large radii may be made with the *Suzaku* Observatory, facilitated by the low internal background and relatively sharp energy resolution of the XIS CCD detectors. In Paper I we derived the abundance pattern in the elliptical galaxy NGC 4472 from analysis of *Suzaku* spectra, supported by analysis of co-spatial *XMM-Newton* Observatory spectra. Application of simple chemical evolution models to these data, led us to conclude that the abundances may be explained by a combination of α-element enhanced stellar mass loss and direct injection of ejecta from SNIa exploding at a rate $\sim 4-6$ times lower than the standard value. In addition, we discovered abundance anomalies in the sense that no published set of SNIa yields could simultaneously reproduce the inferred Ca and Ar, and Ni abundances; and (confirming prior results summarized in Paper I) in the sense that standard core collapse nucleosynthesis models evidently overproduce O by ~ 2.

In this paper we adopt a broadly similar approach in our investigation of NGC 4649 (M60). As is the case for NGC 4472, NGC 4649 is a giant elliptical galaxy in the Virgo cluster with an old stellar population enhanced in α-elements – but with several notable differences both optically and in X-rays. In particular NGC 4649 has a substantial major axis rotation (Brighenti et al. 2009, and references therein), and is considerably more compact in X-rays. We have adjusted our spectral analysis procedures in response to the distinctive X-ray characteristics of NGC 4649, and have revised and expanded our models to consider possible episodes of inflow, and a recently published set of SNIa yields.

We detail our data reduction and spectral analysis procedures in Sections 2 and 3, where we present our derived NGC 4649 hot ISM thermal and chemical properties and their radial variation. In Section 4 we focus on interpreting the global abundance pattern in the context of the relative contributions of metal enrichment from stellar mass return, SNIa, and inflow

of extragalactic material using steady state solutions to the equations of chemical evolution. Section 5 includes a summary of our conclusions, and discusses possible implications of our results. In an appendix we examine the effects of the recent updated atomic database *AtomDB* in spectral fitting of elliptical galaxy hot ISM such as NGC 4649.

2. Construction of NGC 4649 Spectra and Associated Files

2.1. *Suzaku* Spectral Extraction and Preparation

NGC 4649 was observed with *Suzaku* (Mitsuda et al. 2007) between 2006-12-29 and 2007-01-04 (ObsID 801065010), at which time three co-aligned, $17.8' \times 17.8'$ field-of-view X-ray Imaging Spectrometer (XIS) CCD cameras (Koyama et al. 2007) – two front-illuminated (FI: XIS0 and XIS3) and one back-illuminated (BI: XIS1) – were operational, each XIS in the focal plane of an X-ray Telescope (XRT) with a $2'$ half-power diameter (Serlemitsos et al. 2007). Observations were conducted utilizing the space-row charge injection (SCI) technique that reverses the degradation in energy resolution caused by accumulated radiation damage (Nakajima et al. 2008). We initiate our data reduction with the unfiltered event files. These data underwent Version 2.0.6.13 pipeline processing on 2007-08-17 that enables one to properly account for the effect of SCI on instrument characteristics and performance (Uchiyama et al. 2008). We reprocess the unfiltered event files by hand in order to apply updated calibration data and software, following the procedures described in Paper I. We recalculate PI values and grades, select event grades (0, 2, 3, 4, 6) that correspond to X-ray photon events, filter on pixel status (eliminating bad charge transfer efficiency columns, and rows invalidated by the charge injection process) and select good time intervals (GTI) based on pointing, data and telemetry rates, SAA proximity ("SAA_HXD $\equiv 0$, T_SAA_HXD $>$ 436"), and proximity to the earth's limb and illuminated Earth ("ELV > 5, DYE_ELV $>$ 20"). In addition, telemetry-saturated frames and calibration source photons are screened out; and, hot and flickering pixels are removed, and we accept only GTI where the revised geomagnetic cut-off rigidity COR2 > 4, thus eliminating intervals with the highest particle background level (Tawa et al. 2008) without compromising overall statistical accuracy. 5×5 event files are converted to 3×3 mode format, and merged with the 3×3 event files. The exposure times in the cleaned event files are 216.6 (216.5) ks for the XIS0 and XIS3 (XIS1) spectra.

We extract spectra from the inner $8'$ ($\sim 6.5 R_e = 36.2$ kpc at the NGC 4649 distance of 15.6 Mpc; Tonry et al. 2001, where R_e is the optical half-light radius from Bregman, Temi, & Bregman 2006) in $2'$ and $4'$ circular annuli, centered on the NGC 4649 optical nucleus ($\alpha = 12h43m40.0s$, $\delta = +11°33'10''$) that very closely corresponds to the X-ray peak in the

Suzaku image. The spectral redistribution matrix files (**rmf**) are generated using `xisrmfgen` version 2009-02-28. The **rmf** and spectral files are binned to 2048 channels. The effective area function files (**arf**) for the source spectra are generated by the `xissimarfgen` version 2009-01-08 Monte Carlo ray-tracing program (Ishisaki et al. 2007) with 400000 simulation photons per energy bin, and an input source fits image file generated from a β-model fit to the background-subtracted X-ray surface brightness profile extracted from archival *Chandra* data ($\beta = 0.467$, core radius $3.5''$). Spectra from the FI chips, XIS0 and XIS3, are co-added and a weighted XIS0+3 response function calculated from their respective **rmf** and **arf** files. Source spectra are grouped into bins with a minimum of 15 cts, and we derive best-fit parameters and confidence levels using χ^2 statistics. Errors correspond to 90% confidence limits.

The XIS background consists of Non-X-ray (instrumental and charged particle) Background (NXB), Galactic X-ray Background (GXB), and (extragalactic) Cosmic X-ray Background (CXB) components. Since NGC 4649 fills the *Suzaku* field of view, we estimate and subtract the NXB component and include additional components in our spectral fits to account for the GXB and CXB. The NXB component is estimated from observations of the night earth taken in SCI mode within 150 days of the starting or ending dates of our observation using `xisnxbgen` version 2008-03-08. The NXB event list in that time interval undergoes the identical screening as the source data, is sorted by geomagnetic cut-off rigidity, and weighted according to the cut-off rigidity distribution in the source event file (Tawa et al. 2008). The estimated NXB spectra include only those events collected in the regions on the detector from which the source spectra are extracted. Since the CXB and GXB are spatially distributed distinctly from that of the NGC 4649 X-ray emission, a separate **arf** file is generated using 2000000 simulation photons per energy bin from a uniform source of radius $20'$ and applied to the background in spectral fits. Combined XIS0+3 NXB spectra and response functions are constructed as described above.

We display the NXB-subtracted source count rates in each annulus, and the fraction of the total counts in the NXB for the corresponding bandpass used in spectral fitting (see below), in Table 1 .

2.2. *XMM-Newton* EPIC Spectral Extraction and Preparation

NGC 4649 was observed with *XMM-Newton* (Jansen et al. 2001) for ~54 ks on 2001-01-02 (ObsID: 0021540201), and for ~92 ks on 2007-12-19 (ObsID: 0502160101). We downloaded the data from the High Energy Science Archive Research Center (`HEASARC`) data

archive[1] and processed them with Science Analysis System (SAS) version 11.0.1, utilizing the techniques described in Kuntz & Snowden (2008) and Snowden et al. (2008) through application of the *XMM-ESAS* (XMM-Newton Extended Source Analysis Software) suite of procedures. EPIC-MOS and -PN CCD camera photon event files were generated in the standard way with the tasks `emchain` and `epchain`, respectively[2]. Files were processed with $FLAG == 0$, and screened to retain only those events with $PATTERN <= 12$ for the MOS and $PATTERN <= 4$ for the PN.

The event files for each observation was screened for flares by examining their lightcurves using the `xmmlight_clean` scripts (Bauer et al. 2008). The useful exposure times, after cleaning, are ∼49 ks (MOS) and ∼41 ks (PN) for the ObsID 0021540201 event lists, and ∼73 ks (MOS) and ∼70 ks (PN) for the ObsID 0502160101 event lists. *XMM-Newton* observations may be significantly contaminated by soft protons originating in the solar wind (Kuntz & Snowden 2008). Although the lightcurve filtering process largely removes soft proton flares, we determine the level of residual soft proton contamination using the `Fin_over_Fout` method (Molendi, De Luca, & Leccardi 2004). We find the level of contamination to be minor for the MOS detectors, and negligible for the PN detector, during the first (2001) observation. However for the second (2007) observation, although the two MOS cameras again experienced only minor contamination, the PN camera was significantly affected.

The extracted spectra are binned so that each channel has a minimum of 50 counts, and we consider an energy range of 0.3-5.5 keV for the MOS detectors and 0.4-5.5 keV for the PN detector. We extracted spectra from concentric annuli with identical centers and (2′) widths to those of the *Suzaku* extraction regions. The spectral extraction was performed using the *XMM-ESAS* tasks *mos-spectra* and *pn-spectra* for the relevant detectors. These scripts extract the spectra, and generate the instrument response (**rmf** and **arf**) matricies. The tasks *mos-back* and *pn-back* are used to model the instrumental and particle backgrounds (NXB) for each of the extracted spectra.

The source count rates in each annulus are displayed in Table 2.

We use the the `HEASARC` background tool[3] to extract the ROSAT All-Sky Survey (RASS) spectrum from an annular region, with an inner radius of 1° and an outer radius of 2°, centered on the X-ray peak of NGC 4649 – assuming that the average in the annulus is a fair representation of the CXB and GXB at the position of the galaxy. This data is

[1]http://heasarc.gsfc.nasa.gov/docs/archive.html

[2]http://xmm.esac.esa.int/external/xmm_user_support/documentation/sas_usg/USG/

[3]http://heasarc.gsfc.nasa.gov/cgi-bin/Tools/xraybg/xraybg.pl

Table 1. *Suzaku* Count Rates

region	XIS0+3	XIS1
$0-2'$	0.399 (0.008)	0.299 (0.011)
$2-4'$	0.154 (0.058)	0.127 (0.069)
$4-6'$	0.0840 (0.18)	0.0676 (0.21)
$6-8'$	0.0583 (0.18)	0.0522 (0.22)
$4-8'$	0.151 (0.22)	0.124 (0.25)
$2-6'$	0.232 (0.10)	0.189 (0.125)

Note. — Total counts rates in cts s^{-1} in the energy band used for spectral fits (0.4-4.0 keV for the $6-8'$ annulus, 0.4-7.0 keV for all others). Values in parentheses represent the fractions of total counts in the NXB.

Table 2. *XMM-Newton* EPIC Count Rates

region	MOS1	Exposure	MOS2	Exposure	PN	Exposure
			ObsID 0021540201			
$0-2'$	0.518	45.21	0.507	45.54	1.797	49.28
$2-4'$	0.173	···	0.185	···	0.672	···
$4-6'$	0.103	···	0.103	···	0.192	···
$6-8'$	0.067	···	0.059	···	0.313	···
			ObsID 0502160101			
$0-2'$	0.504	67.24	0.482	66.46	1.782	58.25
$2-4'$	0.154	···	0.142	···	0.447	
$4-6'$	0.103	···	0.080	···	0.201	···
$6-8'$	0.056	···	0.057	···	0.128	···

Note. — Total counts rates in cts s^{-1} in the energy band used for spectral fits (0.4-5.5 keV for the PN and 0.3-5.5 keV for the MOS). The exposure time is in units of ks.

simultaneously fit with the EPIC data.

2.3. *XMM-Newton* RGS Spectral Extraction

We extract the RGS spectra for this galaxy using the standard SAS procedures, applying the `rgsproc` task to generate filtered event files and spectra for both observations (OBSID 0021540201 and 0502160101). We exclude some short time intervals where we detected flares in the background light curves, resulting in the exposure times listed in Table 3.

We use the standard background products and generate RGS response matrices using the task *rgsrmfgen* that are technically applicable to spectra of point sources in the RGS field of view. To account for the mixing of spatial and spectral information from extended sources, the matrices are convolved with an image of NGC 4649 (with point-sources removed) created from *Chandra* ACIS-S data (OBSID: 8182) using the `FTOOL` *rgsrmfsmooth*. The image is adaptively smoothed with minimum of 75 counts to reduce the noise prior to the response matrix convolutions.

3. Spectral Analysis

3.1. *Suzaku Spectral Analysis*

We employ XSPEC version 12.7 to simultaneously fit the *Suzaku* XIS0+3 and XIS1 NGC 4649 spectra. Our baseline source model consists of an absorbed single-temperature thermal plasma, plus a 7.5 keV thermal bremsstrahlung component to account for the LMXB (Irwin et al. 2003; Humphrey & Buote 2008). Temperatures and heavy elemental abundances (C, N,

Table 3. *XMM-Newton* RGS Count Rates

region	RGS1	Exposure	RGS2	Exposure	Order
		ObsID 0021540201			
$0-1.'5$	0.064	52.56	0.100	51.08	1
$0-1.'5$	0.026	...	0.028	...	2
		ObsID 0502160101			
$0-1.'5$	0.051	74.73	0.090	74.78	1
$0-1.'5$	0.026	...	0.027	...	2

Note. — Total counts rates in cts s^{-1} for the RGS spectra for each observation. The exposure time is in units of ks.

O, Ne, Mg, Al, Si, S, Ar, Ca, Fe, Ni) in the former component are estimated using the **vapec** model that, in this latest version of XSPEC, incorporates the updated *AtomDB* v2.0.1 atomic database. We note that, at elliptical galaxy X-ray temperatures, spectral fits are significantly impacted by changes with respect to the *AtomDB* v1.3.2 database used in earlier versions of XSPEC (see Appendix A). Therefore, any detailed comparison with previous results (Randall, Sarazin, & Irwin 2004, 2006; Tozuka & Fukazawa 2008; Humphrey et al. 2008; Diehl & Statler 2008; Nagino & Matsushita 2009) are of limited utility, although we note a general $< 4'$ ISM temperature profile consistency if we use *AtomDB* 1.3.2. Addition of a second **vapec** model (with identical abundances) does not improve the fits, and is not further considered. We fix the redshifts of the source components at the value corresponding to the NGC 4649 distance. We apply the Wilms, Allen, & McCray (2000) Tuebingen-Boulder ISM absorption model (**tbabs**), and values in excess of the Galactic value of 2.2×10^{20} cm^{-2} (Dickey & Lockman 1990) are considered as described below. We adopt the Asplund et al. (2009) solar abundance standard, newly implemented in XSPEC 12.6, fixing C and N at their solar values. Since we find that only O, Ne, Mg, Si, S, and Fe are (formally) well-constrained, Al:Mg, Ca:Ar:S, and Ni:Fe are fixed at their solar ratios (Murakami et al. 2011). The models include a constant XIS1/XIS03 multiplicative factor to account for flux calibration offsets that, when fitted for, ranges from 1.0–1.08.

We include four astrophysical background components for all extraction regions, although these are not always formally required for the innermost annuli where the contribution of one or more of these is small or negligible. We model the CXB by an index 1.4 power-law (Kushino et al. 2002), and the GXB by the sum of solar-abundance thermal plasma (**apec**) models representing the Milky Way halo (MWH) and Local Hot Bubble (LHB) (Hayashi et al. 2009; Nagino & Matsushita 2010). The CXB and MWH are absorbed by the Galactic column, the LHB is unabsorbed. We also include an additional extended, 0.5 solar abundance **apec** component (Loewenstein, Valinia, & Mushotzky 2001) to model the Virgo ICM (see, also Buote & Fabian 1998, Randall et al. 2006, 2008, Ji et al. 2009 – hereafter Ji09, and Bogdan & Gilfanov 2011, for evidence of emission from a second, hotter medium). We allow normalizations for these components in each annuli to freely vary in general; however, the MWH/LHB flux ratio is assumed to be constant (see below). We tie the background XIS1-to-XIS0+3 ratio to the value in the source model. Separate **arfs** are applied to background and source model components as described above.

Because the GXB is most prominent in the outermost annuli, we fit the $6 - 8'$ annulus (simultaneously with the RASS spectrum) first to determine the LHB, MWH, and ICM temperatures. The NXB dominates above 4 keV in this annulus, so we fit over the 0.4-4 keV bandpass (all other spectra are fit over 0.4-7 keV). The column density is fixed at the Galactic value, however *post facto* fits with the higher absorption determined from the

innermost annulus (see below) yield virtually identical results. The background-component temperatures in the spectra extracted from other regions are fixed at these outer region best-fit values: kT(LHB) = 0.105, kT(MWH) = 0.187, kT(ICM) = 1.69, as is the MWH/LHB flux ratio (Murakami et al. 2011). Relaxing these constraints did not significantly impact the best-fit ISM parameters.

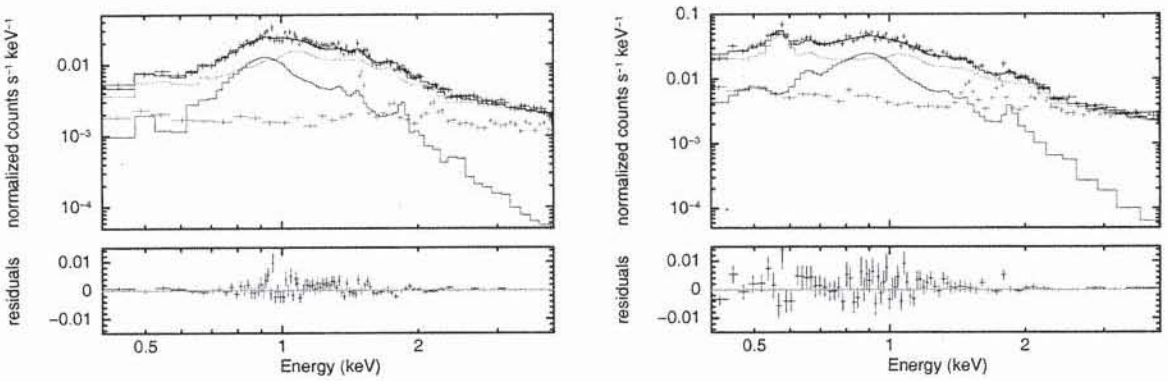

Fig. 1.— $6 - 8'$ aperture *Suzaku* XIS source (NXB-subtracted) spectra and best simultaneous fit models to data from all three detectors (black data points and histogram in top panel), with residuals (bottom panel). Contributions from the ensemble of low mass X-ray binaries (if significant; LMXB, blue), from hot ISM thermal plasma components (red), and from the sum of GXB, CXB, and ICM background components (orange) are separately plotted. The NXB (purple), that is subtracted prior to spectral fitting, is also displayed. The *left* panel (a) shows the sum of the XIS0 and XIS3 spectra, folded through a weighted response, the right panel (b) shows the XIS1 spectrum.

We display the minimized (reduced) χ^2 values, and source model temperatures abundances, and column densities, for each annuli in Table 4; and plot spectra, best-fit models (and their components), and data residuals to the best-fit model for the $2'$ annular partition-

Table 4. *Suzaku* Best-Fit ISM Parameters

region	χ^2/ν	N_H	kT	O	Ne	Mg	Si	S	Fe
$0-2'$	1994/1624	$8.4^{+0.3}_{-0.6}$	$0.867^{+0.003}_{-0.003}$	$0.91^{+0.09}_{-0.12}$	$2.09^{+0.19}_{-0.11}$	$1.14^{+0.05}_{-0.04}$	$1.01^{+0.05}_{-0.034}$	$1.20^{+0.15}_{-0.10}$	$0.99^{+0.02}_{-0.01}$
$2-4'$	1578/1463	$10.0^{+2.3}_{-2.2}$	$0.890^{+0.020}_{-0.016}$	$0.76^{+0.17}_{-0.17}$	$1.24^{+0.24}_{-0.18}$	$0.49^{+0.06}_{-0.07}$	$0.57^{+0.06}_{-0.06}$	$0.76^{+0.16}_{-0.16}$	$0.47^{+0.08}_{-0.04}$
$4-6'$	1529/1449	2.2*	$0.931^{+0.037}_{-0.047}$	$0.91^{+0.42}_{-0.31}$	$0.72^{+0.37}_{-0.50}$	$0.36^{+0.20}_{-0.15}$	$0.62^{+0.18}_{-0.15}$	$0.56^{+0.46}_{-0.43}$	$0.34^{+0.06}_{-0.10}$
$6-8'$	1054/1107	2.2*	$0.871^{+0.083}_{-0.031}$	$0.62^{+0.33}_{-0.46}$	$0.046^{+0.33}_{-0.046}$	$0.21^{+0.15}_{-0.16}$	$0.34^{+0.16}_{-0.17}$	$0.38^{+0.57}_{-0.38}$	$0.15^{+0.09}_{-0.02}$
$2-6'$	2040/1946	$9.7^{+2.6}_{-2.7}$	$0.897^{+0.019}_{-0.018}$	$0.84^{+0.16}_{-0.21}$	$1.01^{+0.23}_{-0.16}$	$0.44^{+0.05}_{-0.07}$	$0.54^{+0.05}_{-0.06}$	$0.68^{+0.15}_{-0.15}$	$0.41^{+0.06}_{-0.03}$
$4-8'$	2019/2018	2.2*	$0.923^{+0.025}_{-0.062}$	$0.68^{+0.32}_{-0.19}$	$0.31^{+0.17}_{-0.22}$	$0.28^{+0.14}_{-0.09}$	$0.44^{+0.17}_{-0.09}$	$0.43^{+0.34}_{-0.29}$	$0.22^{+0.02}_{-0.023}$

Note. — Displayed for each spectral extraction region are minimized χ^2/dof for simultaneous fits to *Suzaku* XIS0, XIS3, and XIS1 spectra, best-fit columns densities (in units of 10^{20} cm^{-2}), best-fit ISM temperatures (in keV), and best-fit O, Ne, Mg, Si, S, and Fe abundances referred to the solar standard of Asplund et al. (2009). Asterisks denote fixed parameters.

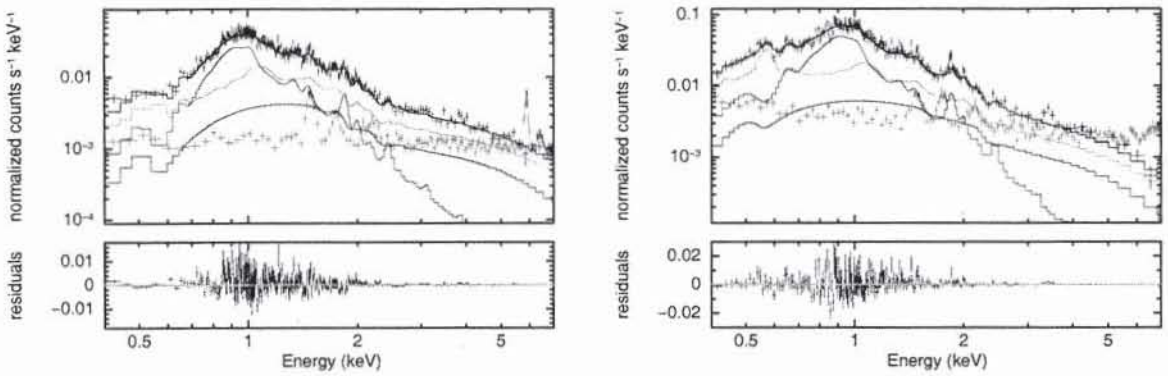

Fig. 2.— Same as Figure 1 for the $4-6'$ aperture.

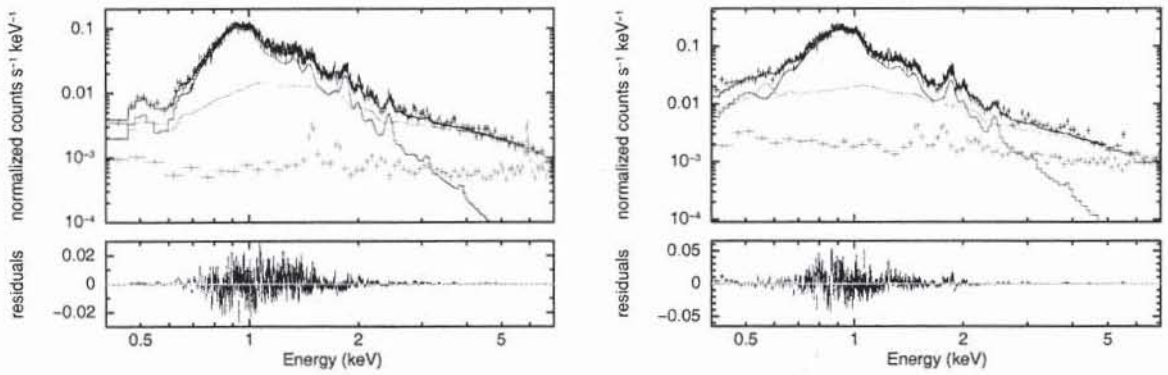

Fig. 3.— Same as Figure 1 for the $2-4'$ aperture.

ing of the $8'$ region in Figures 1-4. We note the following details. We find degeneracies in some fits among the normalizations of the CXB, ICM, and LMXB hard component normalizations (thus the latter component does not appear in Figures 1 and 3); however, these do not introduce significant errors in the hot ISM abundance or temperature determinations. Best-fit model parameters of interest are insensitive to whether thermal bremsstrahlung or power-law models are adopted for LMXB components. We adopt the former since in this case fits are somewhat less sensitive to assumptions about the absorption. In the $0-2'$ region, we found systematic positive residuals at $\sim$ 1.23-1.24 keV that can be well fit by a narrow (*i.e.* unresolved by *Suzaku*) Gaussian emission line. We include this component in the fits plotted and reported here, although the only effect is a reduction of χ^2 (by ~ 100). Excess absorption is strongly required (only) in the inner $4'$ – $\Delta\chi^2 \sim 260$ (26) in the $0-2'$ $(2-4')$ region. The radial variation argues against the cause being incorrect modeling of the contamination of the time-dependent Optical Blocking Filter, which we further confirmed by fitting the $0-2'$ spectra extracted from data reprocessed using a recently updated (2011 June) contaminant model. We have also applied the mixing model in XSPEC (`suzpsf`) that

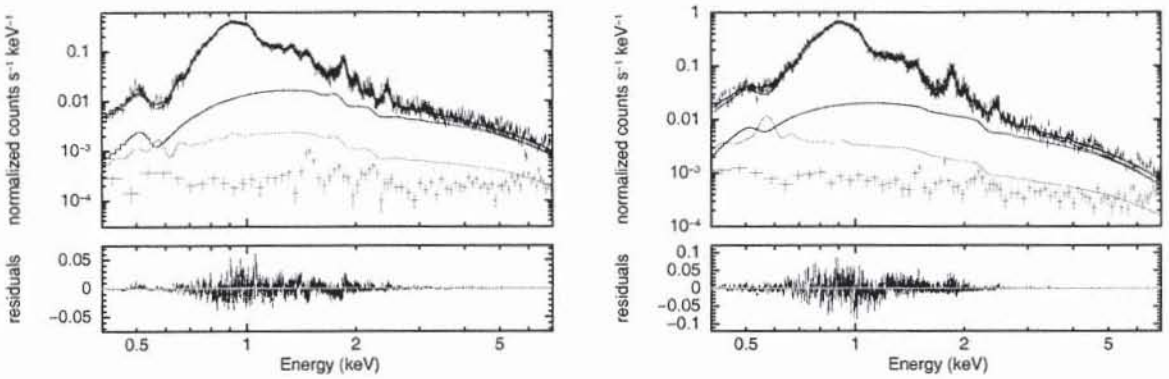

Fig. 4.— Same as Figure 1 for the $0-2'$ aperture.

aims to account for the cross-contamination of spectra due to the broad *Suzaku* point spread function (psf). These solutions tend to be unstable in how the ISM abundances are distributed; however, we note that the emission-averaged abundances over the entire $(0-8')$ region are robust and consistent with those derived from the above fits.

We plot the *Suzaku*-derived abundance profiles of O, Ne, Mg, Si, S, and Fe in Figures 5abc, and abundance ratio profiles (with respect to Fe) in Figures 6ab. Since these profiles are not deprojected, nor corrected for the *Suzaku* point spread function, the true abundance gradients are steeper. There is clearly a negative abundance gradient for Ne, Mg, Si, S, and Fe, and a hint of positive gradients in S/Fe and Si/Fe (Figure 6b).

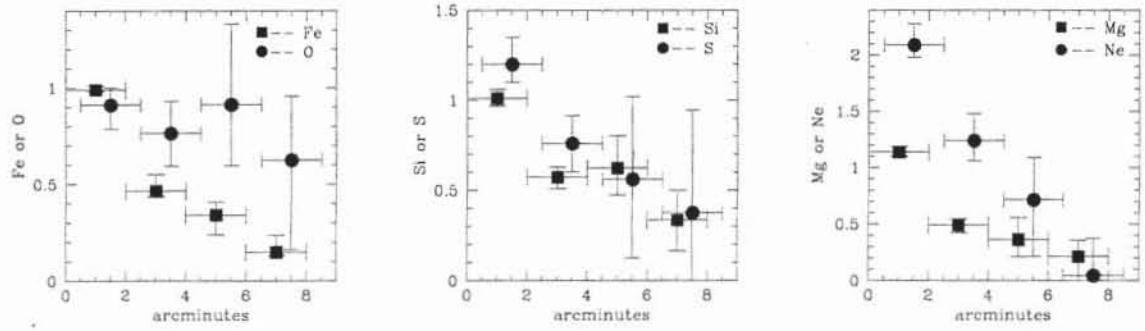

Fig. 5.— Fe and O (*left* panel, (a)), Si and S (*middle* panel, (b)), Mg and Ne (*right* panel, (c)) abundance profiles. The points represented by circles are shifted to the right by $0.5'$.

We plot the *Suzaku*-derived abundance ratios with respect to Fe for the entire galaxy (out to $8'$) in Figure 7, estimated as an emission-measure-weighted average of the $0-2'$, $2-4'$, $4-6'$, and $4-8'$ spectra (consistent results are derived using the $0-2'$, $2-4'$, and $4-8'$ regions, or the $0-2'$, $2-6'$, and $6-8'$ regions). For comparison, the NGC 4472

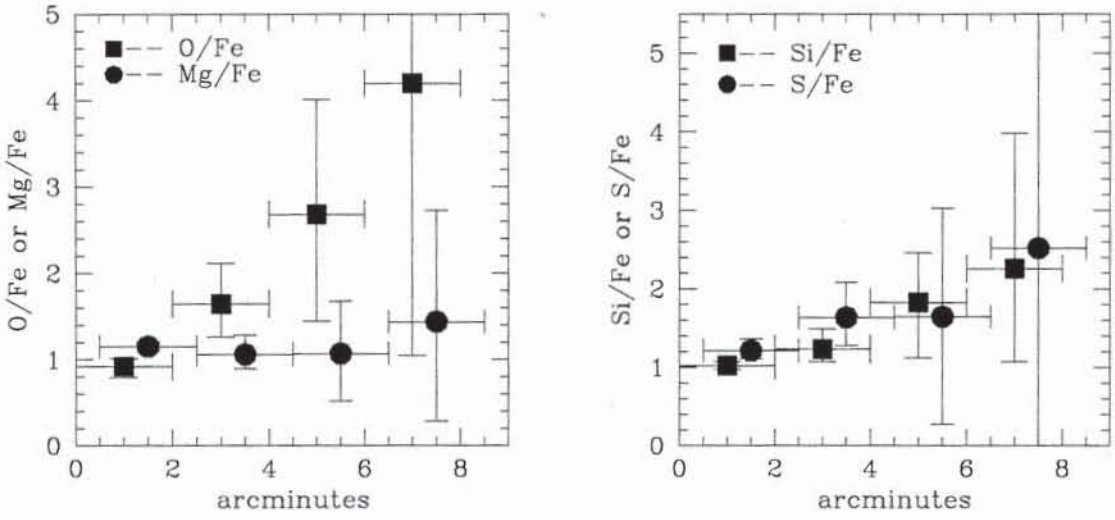

Fig. 6.— Profiles of abundance ratios with respect to Fe for O and Mg (*left* panel, (a)); and, Si and S (*right* panel, (b).

pattern (renormalized to the same solar standard) from Paper I is also shown. The Mg/Fe, Si/Fe, and S/Fe abundance ratios are consistent between the two galaxies, although the more problematic O/Fe and Ne/Fe abundances (O/Fe because of the importance of Galactic halo emission, Ne/Fe because of blending with Fe L) are discordant.

3.2. *XMM-Newton Spectral Analysis and Comparison with Suzaku*

Compared to *Suzaku*, we found the *XMM-Newton* spectral fits considerably more sensitive to the treatment of the (substantially more prominent) background – likely due to the presence of North Polar Spur emission (Randall, Sarazin, & Irwin 2004). In the end, we adopt what may be considered the most conservative approach – confining the fit to the 0.3-5.5 keV band (MOS) or 0.4-5.5 keV band (PN) and, as detailed in the previous section, following the *XMM-ESAS* prescription that exclusively subtracts an estimate of the quiescent particle background. The *XMM-ESAS* generation of instrumental backgrounds does not remove the fluorescent spectral line features; and, some residual soft proton contamination may also be present in the extracted spectra. Thus we include the following additional NXB components in our EPIC spectral models: narrow, fixed-energy Gaussian emission lines corresponding to Al Kα at 1.49 keV (MOS and PN) and Si Kα at 1.75 keV (MOS only) to account for the former; and, a powerlaw with index fixed at 0.3 for the latter. As with the XIS spectral

fits we include thermal components, modeled with the **apec** plasma code, to represent LHB, MWH, and ICM emission, and a power law to account for the unresolved CXB. We again find that the addition of a narrow 1.24 keV line improved fits in the inner region, and this is included in $0-2'$ and $2-4'$ EPIC, as well as RGS, fits.

We display the best-fit model parameters for simultaneous EPIC MOS1, MOS2, and PN $0-2'$ region spectral fits, and also for fits to the RGS spectra, for the combined observations (2001 and 2007) in Table 5. Spectra, best-fit models, and residuals are shown in Figure 8 for the former, and in Figure 9 for the latter. We compare $0-2'$ *Suzaku*, $0-2'$ EPIC, and RGS abundance determinations in Figure 10, finding good agreement in general and excellent agreement with respect to the temperatures and Fe abundances. A discrepancy in the intrinsic absorption persists, with a column density consistent with the Galactic value of 2.2×10^{20} cm^{-2} (Dickey & Lockman 1990) for the EPIC fits. We note that, other than the reduction in goodness-of-fit, fixing the column density in fits to *Suzaku* spectra at the lower Galactic value has little effect on the best-fit parameters – the largest effect is a $\sim 25\%$ reduction in the $0-2'$ O abundance. Fixing the column density in the $0-2'$ EPIC spectra at the best-fit *Suzaku* value of 8.4×10^{20} cm^{-2} does not impact the goodness-of-fit and, likewise, shifts best-fit abundance by $\sim 20\%$ or less. An even smaller effect is found if we restrict the XIS fits to energies > 0.7 keV and fix the column density at the Galactic value.

The results of fitting the EPIC spectra extracted from the $0-2'$, $2-4'$, and $4-6'$ annuli are displayed in Table 6. The higher background in the EPIC cameras did not allow us to successfully fit the 6-8′ annulus. Previous analysis of *XMM-Newton* data (Randall, Sarazin, & Irwin 2006; Nagino & Matsushita 2009; Ji et al. 2009) are generally in agreement with our results although there are some significant discrepancies at some radii. As noted above (Section 3; see, also, Appendix A), comparison is complicated by the recent *AtomDB* update and, in fact, we find fair agreement in the inner regions if we shift to the older *AtomDB* 1.3.2 version and include a second, hotter ISM component (slightly favored in this case). Moreover, these studies employ simpler and less conservative background treatments that utilize subtraction of spectra extracted from "off-source" regions, while we explicitly include GXB and ICM components, allowing for their local variation and that of the instrumental background. For example, our central Fe and O abundances in the inner $2'$ agree well with

Table 5. *XMM-Newton* RGS and EPIC $0-2'$ Best-Fit ISM Thermal Parameters

Spectra	χ^2/ν	kT	O	Ne	Mg	Si	S	Fe	Ni
EPIC (2001+2007)	1756/1202	$0.862^{+0.011}_{-0.004}$	$0.64^{+0.05}_{-0.06}$	$1.52^{+0.18}_{-0.12}$	$1.34^{+0.04}_{-0.05}$	$1.25^{+0.04}_{-0.05}$	$1.41^{+0.11}_{-0.12}$	$0.97^{+0.01}_{-0.01}$	$3.03^{+0.14}_{-0.13}$
RGS (2001+2007)	822/753	$0.866^{+0.020}_{-0.007}$	$1.0^{+0.15}_{-0.15}$	$1.66^{+0.34}_{-0.33}$	$0.94^{+0.30}_{-0.27}$	$1.51^{+0.60}_{-0.57}$	...	$0.97^{+0.07}_{-0.08}$	$2.93^{+0.62}_{-0.56}$

previous work while we find lower Si abundance than (Nagino & Matsushita 2009; Ji et al. 2009) in the same region. In the $2-4'$ and $4-6'$ rings, where the background is more significant, we find higher abundances than these previous works.

We plot the ratio of the EPIC-derived abundances to those of *Suzaku* in Figures 11abc, and the EPIC abundance ratio profiles (with respect to Fe) in Figures 12ab. The latter show a dropoff in the $4-6'$ annulus with respect to the inner $4'$. The EPIC S/Fe and Si/Fe (Figure 11b) profiles echo those seen in the XIS data (Figure 6b) in indicating positive gradients. However, while *XMM-Newton* and *Suzaku* abundances show good agreement in the $0-2'$ and $4-6'$ regions, the EPIC abundances are more discrepant in the $2-4'$ annulus. We have investigated this annulus in more detail by conducting joint EPIC/XIS fits, considering different bandpasses, and examining fits with the absorption column density both free and fixed. In doing so we found that the EPIC spectra admit of two fits of comparable quality – one with Galactic absorption and relatively high abundances (Table 6), one with elevated absorption and lower abundances that is in accord with the *Suzkau* fits (Table 4). However the converse is not true: the XIS spectra are not consistent with the higher abundance model.

Based on the above considerations, we adopt the abundances that we infer from fitting the *Suzaku* spectra for comparison with simple chemical evolution models. These are evidently more robust, for the crude spatial binning that we employ, because of the lower background and sharper energy resolution of *Suzaku* (see Paper I). As a result we extend the measured abundance pattern to greater radii, encompassing a larger fraction of the optical galaxy than was previously possible. A parallel analysis that utilizes the *XMM-Newton* results in the same qualititative results and conclusions.

Table 6. *XMM-Newton* Annular Best-Fit ISM Parameters

region	χ^2/ν	kT	O	Ne	Mg	Si	S	Fe
$0-2'$	1756/1202	$0.862^{+0.011}_{-0.004}$	$0.64^{+0.05}_{-0.06}$	$1.52^{+0.18}_{-0.12}$	$1.34^{+0.04}_{-0.05}$	$1.25^{+0.04}_{-0.05}$	$1.41^{+0.11}_{-0.12}$	$0.97^{+0.01}_{-0.01}$
$2-4'$	1114/910	$0.966^{+0.008}_{-0.015}$	$1.14^{+0.11}_{-0.11}$	$1.23^{+0.71}_{-0.24}$	$1.29^{+0.08}_{-0.19}$	$1.46^{+0.08}_{-0.11}$	$1.27^{+0.22}_{-0.27}$	$1.09^{+0.01}_{-0.03}$
$4-6'$	809/621	$0.960^{+0.032}_{-0.045}$	$0.50^{+0.16}_{-0.16}$	$0.86^{+0.43}_{-0.41}$	$0.31^{+0.22}_{-0.20}$	$0.70^{+0.21}_{-0.12}$	$0.99^{+0.41}_{-0.36}$	$0.45^{+0.12}_{-0.09}$

Note. — Displayed for each spectral extraction region are minimized χ^2/dof for simultaneous fits to *XMM-Newton* EPIC spectra. Shown are best-fit ISM temperatures (in keV), and best-fit O, Ne, Mg, Si, S, and Fe abundances referred to the solar standard of Asplund et al. (2009). The column density is fixed at the Galactic value, 2.2×10^{20} cm^{-2}.

4. Modeling the NGC 4649 Abundance Pattern

Although the host of a weak AGN (Shurkin et al. 2008; Ho et al. 2009; Dunn et al. 2010), NGC 4649 is not strongly disturbed optically (Ferrarese 2006) or in X-rays (Humphrey et al. 2008) and has an old, passively evolving stellar population (Bregman et al. 2006). However, there are strong indications for complex time-dependent circulation flows in the NGC 4649 ISM. On one hand, the thermodynamic characteristics of the gas within 150 pc and the flattened isophotes further out inferred from *Chandra* provide evidence for inflow from kpc scales all the way into the 3×10^9 $M_\odot$ (Humphrey et al. 2008) nuclear black hole (Diehl & Statler 2007; Brighenti et al. 2009). On the other, the fact that this material is rapidly cooling, yet has not appreciably accumulated in the core (in gaseous or stellar form), implies the existence of an outward transport mechanism that is probably intermittent (Brighenti et al. 2009). The impact of these flows on the integrated ISM abundances depends on the metallicity in the flow and its ultimate disposition – in particular whether it escapes the galaxy entirely and permanently.

We utilize the abundance pattern derived from fits to the *Suzaku* spectra in constraining the enrichment of the hot ISM in NGC 4649. We adopt a global perspective in our interpretation of the NGC 4649 abundance pattern by seeking explanation of the hot ISM abundances measured over the entire optical galaxy via X-ray spectroscopy as derived in previous sections, and defer detailed consideration of abundance, and possible abundance ratio, gradients. This is partially driven by the limitations of the *Suzaku* angular resolution, and the attendant degeneracies and uncertainties in spectral modeling, as well as the relative robustness of the galaxy-wide emission averaged abundances (and ratios). Our goal is to examine the overall sources and sinks of the metals measured in this way, and attempt to quantify their relative contributions. In this way, we may identify signatures of the metal transport and enrichment mechanisms discussed above, and better understand the "ins and outs" (Mathews 1990) of the gas flow in this elliptical galaxy.

4.1. Conservation Equations and Steady-State Solution

We proceed with a chemical evolution formalism along the lines of that in Paper I, with the notable additions of explicitly allowing for inflow, and the inclusion of recently published SNIa yields (Maeda et al. 2010). The equations for the conservation of overall ISM mass, $M_{\rm ISM}$, and mass of the *ith* element, $f^i_{\rm ISM} M_{\rm ISM}$, in a fully formed elliptical galaxy are as follows:

$$\frac{dM_{\rm ISM}}{dt} = \dot{M}_{\rm MR} - \dot{M}_{\rm out} + \dot{M}_{\rm in}, \tag{1}$$

and

$$\frac{d(f^i_{\rm ISM} M_{\rm ISM})}{dt} = G^i_{\rm SNIa} + G^i_{\rm MR} - (1 + b^i_{\rm out})\dot{M}_{\rm out} f^i_{\rm ISM} + \dot{M}_{\rm in} f^i_{\rm in}, \tag{2}$$

where $f^i_{\rm ISM}$ is the mass fraction, $\dot{M}_{\rm MR}$ and $G^i_{\rm MR}$ are the mass injection rates for the total gas mass and for the *ith* element from evolved stars, and $G^i_{\rm SNIa}$ the metal mass injection rate from SNIa for the *ith* element. $G^i_{\rm MR} = \dot{M}_{\rm MR} f^i_{\rm stars}$, where $f^i_{\rm stars}$ is the mass fraction of the *ith* element in these mass-losing stars, and $G^i_{\rm SNIa} = \dot{N}_{\rm SNIa} y^i_{\rm SNIa}$, where $\dot{N}_{\rm SNIa}$ is the SNIa rate and $y^i_{\rm SNIa}$ is the *ith* element SNIa mass yield. $\dot{M}_{\rm out}$ ($\dot{M}_{\rm in}$) is the rate of flow out of (into) the system, $b^i_{\rm out}$ a bias factor allowing for an abundance offset for the outflowing gas (Paper I), and $f^i_{\rm in}$ the mass fraction of the *ith* element in the inflowing gas. For a single-phase outflow one expects $b^i_{\rm out} < 0$ as a result of negative abundance gradients in the flow, and $b^i_{\rm out} > 0$ if gas of higher metallicity preferentially exits the galaxy due to buoyancy effects in hot SNIa ejecta (Tang & Wang 2010). For simplicity we assume that $b^i_{\rm out} = b_{\rm out}$ is identical for all elements (Paper I), and that the abundances in the inflow are in the same proportions as in the stars, $f^i_{\rm in} = \phi_{\rm in} f^i_{\rm stars}$.

In the present work we consider equations (1) and (2) in the steady state limit, in which case the source terms may be considered as averages over the density-weighted-mean residence time of the gas. Solving for the ISM abundances,

$$f^i_{\rm ISM} = \frac{f^i_{\rm stars}(1 + r_{\rm in}\phi_{\rm in}) + q y^i_{\rm SNIa}}{(1 + b^i_{\rm out})(1 + r_{\rm in})}, \tag{3}$$

where $r_{\rm in} \equiv \dot{M}_{\rm in}/\dot{M}_{\rm MR} = \dot{M}_{\rm out}/\dot{M}_{\rm MR} - 1$ and $q = 0.00667\theta_{\rm SNIa}/\theta_{\rm MR}\ M_\odot^{-1}$. $\theta_{\rm MR}$ is the specific mass loss rate in units of $2.4 \times 10^{-11}\ M_\odot {\rm yr}^{-1}\ L^{-1}_{B\odot}$ (Paper I), and $\theta_{\rm SNIa}$ is the specific SNIa rate in units of the estimated present-day elliptical galaxy rate of 0.16 SNU[4] (Cappellaro et al. 1997; Cappellaro, Evans, & Turatto 1999; Dilday 2008).

4.2. Source Terms

ISM abundances depend on the ratio $\theta_{\rm SNIa}/\theta_{\rm MR}$ through the parameter q in equation (3). We generally assume $\theta_{\rm MR} = 1$ when quoting values of $\theta_{\rm SNIa}$ based on observationally inferred

[4]SN per century per $10^{10}\ L_{B\odot}$

values of q. The corresponding stellar mass return rate (at the present time), derived in Paper I, is $\sim 40 - 60\%$ times higher than often assumed based on older estimates of turnoff and stellar remnant masses (Faber & Gallagher 1976; Mathews 1989; Ciotti, Pellegrini, & Renzini 1991). $\dot{M}_{\rm MR}$ decreases with time approximately as $t^{-1.3}$ (Paper I), so that the effective value of $\theta_{\rm MR}$ may be greater if some portion of the ISM was lost from stars at an earlier epoch – the average over the past 10 Gyr is 2.2 times the present value. At the same time, estimates of the number of SNIa produced per stellar mass formed ($\sim 0.0005\ M_{\odot}^{-1}$; e.g., Horiuchi and Beacom 2010) result in an average SNIa rate three times our fiducial rate of 0.16 SNU (though $\sim$ half of these may be prompt explosions that are irrelevant for enriching the present-day ISM). Also, a recent estimate of the SNIa rate (Li et al. 2011) is $\sim$twice our fiducial value, and there is evidence of an enhanced rate in clusters (Mannucci et al. 2008; Dilday 2010; Maoz, Sharon, & Gal-Yam 2010). Further complication arises due to the absence of a compelling theoretical explanation for rates as high as these (Ruiter, Belczynski, & Fryer 2009; Mennekens et al. 2010). In other words, $\theta_{\rm SNIa} = \theta_{\rm MR} = 1$ represents a reasonable benchmark but not a strict expectation: the larger values estimated from some optical surveys lack a firm theoretical basis that would indicate the magnitude and evolution of the SNIa rate in any individual elliptical galaxy with its particular structure and stellar population.

In Paper I, individual stellar abundances are determined with reference to a specific SNII yield set (Kobayashi et al. 2006) and the assumption that the SNIa enrichment of the stellar and ISM components are identical; the SNIa/SNII mix was then related to the stellar α/Fe ratio that was allowed to vary. Here we adopt the simpler assumption that stellar O, Ne, Mg, Al, Si, S, and Ar abundances are in solar proportions and overabundant with respect to Ca, Fe, and Ni by a fixed, constant factor given by the α/Fe ratio. We base this on the consistency we found in Paper I between the optically measured $[\alpha/Fe]_{\rm stars}$ and those in our best-fit models to the hot ISM abundance pattern in NGC 4472. Moreover, there is no consensus as to which of the many available SNII yield sets (if any) is appropriate (Gibson, Loewenstein, & Mushotzky 1997; Romano et al. 2010), especially given the uncertainties in, e.g., the initial mass function of the original stellar population and the possibility that SNII yields vary as the metallicity of the stellar population that provides the Type II progenitors accumulates. There is also the possibility that the primordial enrichment of the stars and the ongoing enrichment of the hot ISM are characterized by distinct yields from separate components of a bimodal populations of SNIa (Mannucci, Della Valle, & Panagia 2006; Maoz et al. 2011; Horiuchi & Beacom 2010) or, as may be the case with SNII, that SNIa yields evolve with the progenitor population – in their case due to effects of age and metallicity on the deflagration-to-detonation transition density (Bravo et al. 2010; Krueger et al. 2010; Jackson et al. 2010).

In this way, we focus on the period subsequent to the epoch of formation of the bulk

of the stars, and only assume that an old stellar population with the optically estimated $[\alpha/Fe]_{\rm stars}$ has emerged during the unspecified prior evolution. However, one must keep in mind that there is evidence that individual α-elements deviate from solar ratios in massive ellipticals, and do not vary in lockstep in general (Graves et al. 2007, Smith et al. 2009, and references therein) – in fact our grouping of Ca with Fe above is based on just such evidence for that element (see, also, Pipino & Matteucci 2004; de Plaa et al. 2007). Following Humphrey & Buote (2006); Humphrey et al. (2008), we estimate the following global stellar values from measurements of optical line indices (Trager et al. 2000a,b; Thomas et al. 2005; Howell 2005; Sanchez-Blazquez et al. 2006): $[Fe/H]_{\rm stars} = 0 \pm 0.2$ and $[\alpha/Fe]_{\rm stars} = 0.25 \pm 0.05$, and adopt $[\alpha/Fe]_{\rm stars} = 0.25$. The only relevant supernova yields are those of SNIa that explode after long (>Gyr) evolutionary delay times. We consider a wide range of published SNIa yield sets, including those derived from the W7 (Nomoto et al. 1997) and more recent C-DEF (Maeda et al. 2010) pure deflagration models, and those based on one-dimensional delayed detonation (DD) models with a range of central and transition densities (Nomoto et al. 1997; Iwamoto et al. 1999). For the first time, we consider the yields based on the two- dimensional DD models of Maeda et al. (2010), including their off-center DD model (O-DDT).

Finally, in comparing our models with the NGC 4649 ISM abundance pattern we consider only elements that have distinct and well-measured emission features in the X-ray spectra – O, Mg, Si, S, and Fe – although we also plot Ne when displaying this comparison.

4.3. Solutions Applied to NGC 4649

We consider two classes of simplified solutions to equation (3) for illustrative purposes. In the first the SNIa rate is set to 0 ($q = 0$) so that ISM abundances are proportional to stellar abundances. Figure 13a includes a comparison of the hot ISM and stellar abundance patterns for solar and half-solar stellar Fe abundances ($[Fe/H]_{\rm stars} = 0$, -0.3). Also displayed is the best-fit model including SNIa with $\theta_{\rm SNIa}/\theta_{\rm MR} = 1$: the $[Fe/H]_{\rm stars} = -0.3$ C-DEF model (where SNIa yields for relevant elements are lowest). Notably, abundances are generally overpredicted – even for the $[Fe/H]_{\rm stars} = -0.3$ model with no SNIa.

We now turn to more general steady state solutions. Once the stellar abundance ratios and SNIa yields are specified, the ISM abundance ratios depend on a single parameter. Adopting Fe as a reference element, the ratios are determined by the following:

$$\frac{f^i_{\rm ISM}}{f^{\rm Fe}_{\rm ISM}} = \frac{f^i_{\rm stars}/f^{\rm Fe}_{\rm stars} + py^i_{\rm SNIa}}{1 + py^{\rm Fe}_{\rm SNIa}}, \tag{4}$$

for each element i, where $f^i_{\rm stars}/f^{\rm Fe}_{\rm stars}$ is the corresponding stellar ratio (the solar ratio for Ca

and Ni, and 1.8 times the solar ratio otherwise; see above), and $p \equiv q(1 + r_{\rm in}\phi_{\rm in})^{-1}/f^{\rm Fe}_{\rm stars}$. Essentially, this expresses the simple dependence of the ISM ratios on the ratio of SNIa-to-stellar direct injection, modified by inflow (for $r_{\rm in} > 0$); a uniformly biased outflow does not affect the ratios.

We determine the best-fit (minimum χ^2) value of p to the observed NGC 4649 abundance ratios for each yield set. Figure 13b shows the corresponding abundance patterns for the more recently published yields compared to the observations. Many of the yield sets provide good fits to the abundance ratios (as does the W7 model); the exception being the Maeda et al. (2010) C-DDT model with its exceptionally high Si-to-Fe ratio. We do not find evidence for the oft-reported underabundance of O (see Paper I, and references therein) – in part because of the lower solar standard O abundances in Asplund et al. (2009) that we adopt.

4.4. Discussion

4.4.1. Astrophysical Interpretation of Successful Models

How do the dimensionless model solutions that match the observed hot ISM abundances translate into astrophysical quantities of interest, and are these reasonable? We address that in this subsection by unfolding the single model parameter p into the implied range in the combination of inflow, outflow, and SNIa properties in NGC 4649. The value of p, determined by the observed abundance ratios, determines the relation between the inflow term $r_{\rm in}\phi_{\rm in}$ and the SNIa-to-stellar-mass-return ratio term q (see above), and sets a minimum value of q ($q_{\rm min}$) such that $r_{\rm in}\phi_{\rm in} > 0$: $q_{\rm min} = p f^{\rm Fe}_{\rm stars}$. If one then specifies $f^{\rm Fe}_{\rm ISM}$ one may separately derive $r_{\rm in}$ and $\phi_{\rm in}$ for a given outflow bias parameter, $b_{\rm out}$. The minimum value of q required for $r_{\rm in} > 0$ *and* $\phi_{\rm in} > 0$ is $q_{\rm min} = max[p f^{\rm Fe}_{\rm stars}, (1 + b_{\rm out}) p f^{\rm Fe}_{\rm ISM}/(1 + p y_{\rm SNIa})]$. In what follows we set $\theta_{\rm MR} = 1$ when quoting values of $\theta_{\rm SNIa}$ (i.e., $\theta_{\rm SNIa} = 150q$), and assume $[Fe/H]_{\rm stars} = 0.0$, unless otherwise specified. For illustrative purposes we adopt a composite model with equal contributions from C-DEF, O-DDT, and WDD3 SNIa (Figure 13b); the following discussion is qualitatively unaltered, and the goodness-of-fit similar, for any of the individual well-fitting models. The abundance pattern inferred from optimizing the match to the data over the parameter p for this composite model is shown in Figure 14, where it is compared with the pure stellar and SNIa ratios, as well as the predicted ratio for $\theta_{\rm SNIa} = 1$ and no inflow ($r_{\rm in}\phi_{\rm in} = 0$). The theoretical pattern is extended to the additional elements C, N, Al, Cr, Mn, and Ni (stellar abundances of the former three are assumed equal to those of O-through-Ar, the latter three those of Ca and Fe; see Section 4.1.2). Figure 15a plots $r_{\rm in}\phi_{\rm in}$ as a function of $\theta_{\rm SNIa}$ for this optimum composite model (solid line in Figure 14). The minimum SNIa rate ($r_{\rm in}\phi_{\rm in} \rightarrow 0$), set by the lower value of $[\alpha/Fe]$ in the ISM compared to the stars, corresponds

to $\theta_{\rm SNIa,min} = 0.18$ (0.091 for $[Fe/H]_{\rm stars} = -0.3$); more generically $\theta_{\rm SNIa} > 0.12$ for all of the well-fitting individual SNIa yield sets (for $[Fe/H]_{\rm stars} = 0.0$). The curves in Figure 15a may be expressed as $\theta_{\rm SNIa} = \theta_{\rm SNIa,min}(r_{\rm in}\phi_{\rm in} + 1)$. That is, very large inflow rates are required to reconcile the NGC 4649 ISM abundances with $\theta_{\rm SNIa} = 1$.

In Figure 15b, $r_{\rm in}$ and $\phi_{\rm in}$ are separately broken out based on the measured ∼half-solar global value of $f_{\rm ISM}^{\rm Fe}$ derived from the *Suzaku* spectral fits. The inferred abundances in the accreted gas are < 0.28 times the (nearly solar) stellar value for $\theta_{\rm SNIa} < 1$, reasonable for an intracluster or intragroup medium – and consistent with the outermost *Suzaku* annulus $(6 - 8')$ abundance (Table 3), while $r_{\rm in} > 2.1$. The introduction of a biased outflow that preferentially carries metals out of the galaxy naturally reduces the require inflow rates. For $b_{\rm out} = 1$ (abundances in the outflow twice that in the stars), the inflow metallicity simply shifts to lower inflow rates (Figure 16b) – for fixed $\theta_{\rm SNIa} < 1$ $r_{\rm in} \rightarrow (r_{\rm in} - 1)/2$; more generally, $r_{\rm in} \rightarrow (r_{\rm in} - b_{\rm out})/(1 + b_{\rm out})$ (with a compensating increase in $\phi_{\rm in}$ since $r_{\rm in}\phi_{\rm in}$ is independent of $b_{\rm out}$). For $[Fe/H]_{\rm stars} = -0.3$ the required level of inflow enrichment is higher for a given SNIa rate (Figure 15a) – $r_{\rm in}$ is independent of $[Fe/H]_{\rm stars}$; for $[Fe/H]_{\rm stars} \rightarrow [Fe/H]'_{\rm stars}$ $\phi \rightarrow [(r_{\rm in}\phi_{\rm in} + 1)([Fe/H]'_{\rm stars}/[Fe/H]_{\rm stars}) - 1]r_{\rm in}^{-1}$.

The relative importance of dilution is expected to increase with radius as the timescale to replenish the ISM via stellar mass increases. We do not account for this, but will address this with future multizone models.

4.4.2. NGC 4472 and Other Ellipticals (Briefly) Revisited

As noted above (Figure 10), the abundance *ratio* patterns are generally consistent between NGC 4472 and NGC 4649. This suggests that the higher abundance of Fe in the former is not simply due to a higher SNIa rate – which would skew the abundance pattern – but, in the context of the models described above, may be explained by either more efficient removal of enriched gas or a higher average inflow rate of relatively unenriched gas in the latter. In general, the level and pattern of abundances for other elliptical galaxies observed with *Suzaku* are near solar (Matsushita et al. 2007; Tawara et al. 2008; Komiyama et al. 2009; Sato et al. 2009; Hayashi et al. 2009) – similar to what we report here for NGC 4649, indicating that our simple models may be widely applicable in accounting for the origins of ISM metals in elliptical galaxies. A more thorough analysis that compares and contrasts elliptical galaxy ISM abundances in the context of their environments and intrinsic properties is beyond the scope of this paper, but is currently being pursued. In particular, a larger sample may help in evaluating which SNIa yield set is favored by the X-ray data (next section). An abundance pattern that displayed a lower level of dilution would be helpful in

this regard. A variation (or lack, thereof) in the magnitude of dilution from galaxy to galaxy constrains the nature of the inflow and its relation to elliptical galaxy evolution (see below).

4.4.3. The Significance of Ni

With the effects of SNIa diluted by inflow, it becomes more challenging to use ISM abundances in ellipticals to constrain SNIa yields. Even so, predictions for the pattern among the Fe group elements are sufficiently distinctive that some signature remains, as we illustrate in Figure 16 for the models in Figure 13b. In particular, the Ni abundance (both its absolute value, and that relative to Fe and other elements) is a diagnostic of both the level of SNIa enrichment and of the SNIa nucleosynthesis prescription (see also Paper I, PM11). Also plotted in Figure 16 are the Ni/Fe ratios for fits to RGS and XIS $0-2'$ spectra where the Ni abundance is allowed to float. At the $\sim$keV temperatures of elliptical galaxies, these are determined by fitting the shape of the spectrum in the region where various Fe L (and Ni L) features are generally blended. As a result, there are concerns that these measurements may not be robust to assumptions and uncertainties in the plasma code atomic physics input implemented in spectral fitting packages such as XSPEC. As such it will crucial to confirm the high Ni abundance estimated in this work, Paper I, Ji09, etc. with future high energy resolution X-ray imaging spectroscopic observations, such as those to be conducted by *Astro-H*, and to improve the accuracy of thermal plasma modeling of Ni L.

5. Summary and Implications: Results from X-ray Spectroscopy of NGC 4649 in the Broader Context of Elliptical Galaxy Studies

The distinctive history of giant elliptical galaxies results in the creation and maintenance of an extensive ISM, dominated by hot gas, that contains a fossil record of that very history: evolution determines ecology, ecology enables archeology, archeology illuminates evolution. Based on estimates of supersolar stellar α-to-Fe ratios and SNIa rates in excess of > 0.1 SNU, one naively expects an ISM abundance pattern in elliptical galaxies that is supersolar across the board, and increasingly so for elements more proficiently synthesized in SNIa. In actuality, measured ISM abundances are solar or subsolar for all elements and do not deviate strongly from solar ratios, possibly excepting Ni. A simple reduction in the SNIa rate (or by assuming that SNIa ejecta fail to mix into the hot ISM; Brighenti & Mathews 2005) does not resolve this puzzle – the effective rate would need be reduced to very low values to explain the modest Fe abundance *level*, begging explanation for why the *ratios* do not then mirror the α-element enhanced pattern in the mass-losing stars.

We bring these issues into sharper focus, and attempt to make progress on their resolution, through measurement of the abundance pattern in the elliptical galaxy NGC 4649 derived from deep *Suzaku* and *XMM-Newton* observations. The measurement of abundances in the hot ISM of elliptical galaxies remains problematic, despite the high quality of the spectra extracted from these data due to effects of angular resolution in the case of *Suzaku*, background systematics in the case of *XMM-Newton*, and lingering atomic physics uncertainties (see Appendix A). Nevertheless, by demanding a degree of cross-mission consistency, and focusing most on conclusions that rely on relatively model-independent abundance ratios integrated over the galaxy, we find that robust, and surprising, constraints on elliptical galaxy evolution can be inferred. Towards this end, we compare the galaxy-wide average ISM abundance pattern with one-zone steady state solutions to the equations of chemical evolution that depend on a single parameter that characterizes the relative contributions of SNIa, stellar mass loss, and inflow to the ISM metal inventory. We vary this parameter to fit the data, utilizing the most recent solar standard abundance scale (Asplund et al. 2009) and SNIa yields (Maeda et al. 2010), and reproduce the observed abundance pattern in NGC 4649. This approach lends insight into the contributions of various sources of ISM metal enrichment, even though it is unlikely that the gas is precisely in a steady state at any time.

We find that a key ingredient in models that successfully reproduce the observed pattern is inflow of subsolar metallicity extragalactic gas with an (assumed) abundance pattern similar to that in the stars at an average rate comparable to, or greater than, that of stellar mass loss. Inflow both reduces the overall ISM metallicity and dilutes the effect of Fe group enhancement from direct SNIa injection. Although effective SNIa rates of 0.1 SNU or more are not required, we now find that they may be accommodated (and, in fact, that specific rates < 0.02 SNU are excluded by limits on the ISM $[\alpha/Fe]$ ratio relative to that in the stars) provided that a significant fraction of the ISM is of external origin. Astrophysically reasonable magnitudes of SNIa enrichment and external dilution may play off against one another, as shown in Figure 15, to produce subsolar abundances in roughly solar proportions as observed. In a similar vein, Brighenti et al. (2009) modeled the two-dimensional gasdynamics of NGC 4649 and found that inflow of circumgalactic gas with metallicity comparable to the mean stellar value could dilute the effects of SNIa enrichment (in their models, $\theta_{\rm SNIa}/\theta_{\rm MR} = 0.84$ using our scale) on the Fe abundance by a factor of ~ 3. We cannot precisely identify the origin and means of delivery of the extragalactic material. Inflow may be quasi-steady, or intermittent following the episodes of outflow that must occur to prevent the gas from accumulating to levels beyond what is observed (Colavitti, Pipino, & Matteucci 2009).

The reservoir from which gas accretes may be an intracluster, intragroup, or filamentary intergalactic medium; and may have been previously ejected from the same galaxy (or other

galaxies). Alternatively, the extragalactic material may originate in discrete instances of galaxy merging with gas-rich systems. Some combination of these mechanisms would seem most likely, with their relative importance depending on galaxy history and environment (La Barbera et al. 2011). The level and pattern of ISM metal enrichment will reflect this and, with detailed modeling and additional observational analysis, may prove an important diagnostic of the nature of post-formation elliptical galaxy interactions.

Thus, the X-ray abundance pattern confirms the complex flow and enrichment history of NGC 4649 proposed in Brighenti et al. (2009), and reflects the dynamic, continually evolving nature of elliptical galaxies implied by optical observations (Faber et al. 2007). The earliest epochs of elliptical galaxy formation are characterized by the interplay of major mergers, inflow of primordial gas, vigorous star formation, and powerful outflows (Colavitti, Pipino, & Matteucci 2009; Mannucci et al. 2010; Arrigoni et al. 2010). Even after the quenching of star formation has halted the main formation epoch, ellipticals do not evolve purely in a passive manner in isolation (Thomas et al. 2010). Evidence of mergers and other interactions, indicate that ellipticals continue to grow up to the present day (Trager et al. 2000b; van Dokkum et al. 2008; Tal et al. 2009), as required to explain the observed increase in the size of ellipticals and the continual build up of the red sequence (Naab, Johansson, & Ostriker 2009; van der Wel et al. 2009; Shankar et al. 2010; Robaina et al. 2010; Trujillo, Ferreras, & de La Rosa 2011; Damjanov et al. 2011; Cassata et al. 2011). In addition, there are signs of the presence of modest amounts of more recently formed stars – often in ellipticals with morphological signs of interaction (Trager et al. 2000b; Kaviraj et al. 2008, 2009; Sanchez-Blazquez et al. 2009; Kaviraj 2010; Vega et al. 2010). However, evolution subsequent to the primary star forming epoch must proceed in such a way as to be consistent with the old and passively evolving nature of elliptical galaxy stellar populations inferred from their individual properties and scaling relations (Pipino & Matteucci 2006, 2008). Attempts to resolve this apparent paradox, alluded to in the introduction, often appeal to the process of "dry" merging (Tal et al. 2009; Kaviraj 2010; Cooper et al. 2011) that involves very little gas – and hence new star formation (as contrasted with the $z > 2$ "wet" mergers where stars are efficiently formed). The observed scaling relations and predominance of old stellar populations are thus preserved. However it is not clear that mergers of this type occur in sufficient numbers (Hopkins et al. 2010); and, most galaxies interacting with ellipticals are not, in fact, gas-free (De Propris et al. 2010; Serra & Oosterloo 2010).

Massive elliptical galaxies are themselves not gas-poor, and the observed properties of the hot ISM are often neglected in these considerations. We have shown that the chemical structure of the hot ISM in ellipticals not only confirms a continual environmental impact, but demonstrates that the accreted gas is hot or is heated as it is introduced and interacts with pre-existing hot gas. This implies a reduction of the star formation efficiency of cold

gas that is newly introduced either in the form of mergers with small gas-rich galaxies or via a smoother accretion process (Keres et al. 2009). This accords well with the formalism of prolonged quenching via gravitational heating developed by Birnboim and Dekel (Dekel & Birnboim 2008; Birnboim & Dekel 2011); see also Nipoti & Binney (2007); Johansson, Naab, & Ostriker (2009). A mechanism of this type naturally sets a common dark matter halo mass threshold that corresponds to truncation of the blue cloud and the transition mass between boxy and disky ellipticals (Cattaneo et al. 2009), and (perhaps abetted by the reactivation of an AGN) may continue in some form as a secular means of supressing star formation. The entire one-dimensional "humidity-based" classification of mergers[5] implicitly assumes a one-to-one correspondence between gas content, dissipation, and star formation that breaks down in giant ellipticals known to be filled with hot gas. An encounter involving such a galaxy is never gas-poor, and may involve substantial dissipation if the companion galaxy is also gas-rich. However, these mergers may prove to be a hostile setting for new star formation, and are effectively "dry." Alternatively, the late-time accretion may be dominated by hot mode accretion (van de Voort, et al. 2011). Understanding elliptical galaxy evolution requires tracking the three "phases" of baryonic matter – stars, (cold) star-forming gas, and (hot) inert gas – and how their mutual exchange of mass, metals, and energy as a function of age, environment, and type of merger proceeds as the galaxy evolves subject to internal and external influences (De Lucia et al. 2010; Lu et al. 2011).

Our conclusions are driven by the robust analysis results indicating that ISM abundances are solar or less with ratios that lie between the α-element enriched pattern expected from pure enrichment from stellar mass loss and the O/Ne/Mg-poor pattern expected from the combination of stellar mass loss and direct SNIa injection at $\theta_{\rm SNIa} \sim 1$. As NGC 4649 is a member of the Virgo Cluster and displays a compact X-ray morphology, the evolution of its hot ISM (e.g., stripping of the outer regions) may be affected by the interaction of the galaxy (or a subgroup to which it belongs) with the ICM. Nevertheless, given the universality of the departure of observed elliptical galaxy hot ISM abundances from the naive expectations described above, we suggest that the following main conclusions we draw for NGC 4649 may be generalized:

- ISM abundance patterns indicate that metal enrichment from stellar mass loss and from direct injection of SNIa, and dilution from infall are all significant when averaged over the residence time of the ISM. SNIa injection prevents the ISM from reflecting the supersolar stellar $[\alpha/Fe]$ ratio, and infall dilutes the overall ISM metallicity.

[5]in addition to "wet" and "dry", mergers have also been referred to as "moist" (Sanchez-Blazquez et al. 2009) and "damp" (Forbes et al. 2007)

- The amount of accreted gas must exceed that originating in stellar mass loss rate if one is to reconcile the ISM Fe abundance with the standard specific SNIa rate of 0.16 SNU.
- The success of our models lend further support to the picture of ellipticals as "open ecosystems" that continually grow, and exchange mass and metals with the intergalactic environment and/or other galaxies.
- Our inference that accreted gas mixes in the with the hot ISM may help explain why these processes are accompanied by little or no star formation.

We are grateful Adam Foster, and Randall Smith for their input regarding atomic physics issues. This work could not have been completed without support from NASA *ADAP*, and *Suzaku* and *XMM-Newton* GO programs.

A. Everything You know is Wrong: Effects of Updating the Atomic Database

We initiated analysis of NGC 4649 utilizing the *AtomDB* v1.3.2 data base as implemented in XSPEC version 12.6. Subsequently, with the availability of the updated *AtomDB* v2.0.1 it became evident that the previous best fit models were no longer statistically acceptable due to severe differences in Fe L-shell strength predictions. This is primarily due to differences in the calculated ionization balance of Fe (Adam Foster, private communication). In this appendix we conduct simple illustrative numerical experiments to explore the effect of using the "wrong" database to fit spectra, at CCD energy resolution, of thermal plasmas with $kT \sim 1$ keV. We find significant discrepancies for $kT < 1.3$ keV that – to the extent that the update represents a better description of nature – casts doubt on the accuracy of previous X-ray results for elliptical galaxies and other ∼keV astrophysical plasmas. The resulting artifacts include mis-estimates of the plasma temperature and metal abundances, and false statistical preference for two temperatures.

First we construct simulated spectra, using the NGC 4649 $0-2'$ background and response files. These spectra are normalized to yield 10000 source counts, and are modeled as a solar abundance (Asplund et al. 2009), single-temperature thermal plasma according to *AtomDB* v2.0.1. These are then fit with (one- and two-temperature) models that instead utilize *AtomDB* v1.3.2, and 90% confidence regions derived by cycling through 1000 such realizations. As a control, the identical experiment is conducted by repeating with *AtomDB* v2.0.1 fits. Temperatures of 0.3-2.0 keV are considered.

The ratios, with respect to the input temperature $kT_{in,2.0.1}$, of the best-fit *AtomDB* v1.3.2 temperature $kT_{out,1.3.2}$, are shown in Figure 17a; $kT_{out,1.3.2}$ versus the best-fit control temperature $kT_{out,2.0.1}$ in Figure 17b. Figure 18 shows the ratio of the best-fit Fe abundance in the *AtomDB* v1.3.2 fits to those in the control fits. Other elements show similar behavior, with larger errorbars. Clearly, temperatures and abundances are underestimated relative to their "true" values, with the effect most prominent between 0.5 and 1 keV.

In addition, the goodness-of-fit statistic using the "incorrect" plasma model is significantly worse relative to the control fits for $kT < 1.3$ keV, as shown in Figure 19a. Given that the resulting reduced-χ^2 (χ^2/ν) generally significantly exceeds one, standard procedure is to add an additional component. We conduct an experiment along these lines as well for simulation input temperatures of 0.8, 0.9, 1.0, 1.1 keV and find that, indeed, χ^2/ν generally declines (except for $kT_{in,2.0.1} = 1.1$) and attains acceptable magnitudes ~ 1.1 when an additional hotter ($\sim 1.2 - 1.6$) temperature component is considered. This also converts what had been an abundance *underestimate* for one-temperature models using the "wrong" plasma model into an abundance *overestimate*, as demonstrated for Fe in Figure 19b.

Based on these simple, illustrative numerical experiences we may conclude that deficiencies in the earlier versions of *AtomDB* that includes the **apec** thermal plasma model output spectra, likely resulted in temperature underestimates by as much as 15%. Metal abundance estimates were underestimated for single-temperature models, and overestimated for two-temperature models – where the latter would have been artificially preferred based on goodness-of-fit statistics. The effect, while not monotonic with temperature, is most significant for "true" temperatures ~0.5-1 keV.

Of course, while *AtomDB* v2.0.1 is surely more accurate than its predecessors various, instances of incompleteness and approximation necessarily remain,[6] begging the question of the accuracy of model parameters obtained in current spectral fits.

When models of astrophysical plasma spectra are formally unacceptable, this may be attributed to complexities in the physical conditions or to inaccuracies in the plasma model. Distinguishing these explanations is facilitated by improvements in the quality of atomic databases and X-ray spectra. At the same time, confrontation between the models and data can point the way to improvements in the accuracy of both our understanding of the plasma physical conditions and the key remaining deficiencies in the atomic database and its application.

---

[6]http://www.atomdb.org/

REFERENCES

Arrigoni, M., Trager, S. C., Somerville, R. S., & Gibson, B. K. 2010, MNRAS, 402, 173

Asplund M., Grevesse N., Sauval A.J. & Scott P. 2009, ARA&A, 47, 481

Bauer, M., Pietsch, W., Trinchieri, G., Breitschwerdt, D., Ehle, M., Freyberg, M. J. & Read, A. M., 2008, A&A, 489, 1029

Birnboim, Y. & Dekel, A. 2011, MNRAS, 415, 2566

Bogdan, A., & Gilfanov, M. 2011, MNRAS, in press (arXiv:1106.3435)

Brandt, T. D., Tojeiro, R., Aubourg, E., Heavens, A., Jimenez, R., & Strauss, M. A. 2010, AJ, 140, 804

Bravo, E., Domnguez, I., Badenes, C., Piersanti, L., & Straniero, O. 2010, ApJ, 711, L66

Bregman, J. N., Temi, P., & Bregman, J. D. 2006, ApJ, 647, 265

Brighenti, F. Mathews, & W. G. 2003, ApJ, 587, 580

Brighenti, F. Mathews, & W. G. 2005, ApJ, 630, 864

Brighenti, F., W. G.., Humphrey, P. J., & Buote, D. A. 2009, ApJ, 705, 1672

Buote, D. A. 2000, MNRAS, 311, 176

Buote, D. A., & Fabian, A. C. 1998, MNRAS, 296, 977

Cappellaro, E., Turatto, M., Tsvetkov, D. Yu., Bartunov, O. S., Pollas, C., Evans, R., & Hamuy, M. 1997, A&A, 322, 431

Cappellaro, E., Evans, R., & Turatto, M. 1999, A&A, 351, 459

Cattaneo, A., et al. 2009, Nature, 460, 213

Cassata, P. et al. 2011, ApJ, submitted (arXiv:1106.4308) Cattaneo, A., Dekel, A., Faber, S. M., & Guiderdoni, B. 2009, MNRAS, 389, 567

Ciotti L., D'Ercole A., Pellegrini S., & Renzini A. 1991, ApJ, 376, 380

Ciotti, L., Ostriker, J. P., & Proga, D. 2010, ApJ, 717, 708

Colavitti, E., Pipino, A., & Matteucci, F. 2009, A&A, 499, 409

Cooper, M. C. et al. 2011, ApJ, submitted (arXiv:1109.5698)

Damjanov, I. et al. 2011, ApJ, submitted (arXiv:1108.0656) Colavitti, E., Pipino, A., & Matteucci, F. 2009, A&A, 499, 409

Davé, R., Finlator, K. & Oppenheimer, B. D., MNRAS, 416, 1354

DeBuhr, J., Quataert, E., & Ma, Chung-P., MNRAS, 412, 1341 (arXiv:1107.5579)

De Lucia, G., Boylan-Kolchin, M., Benson, A. J., Fontanot, F., & Monaco, P. 2010, MNRAS, 406, 1533

de Plaa, J., Werner, N., Bleeker, J. A. M., Vink, J., Kaastra, J. S., & Mendez, M. 2007, A&A, 465, 345

De Propris, R., Driver, S. P., Colless, M., Drinkwater, M. J., Loveday, J., Ross, N. P., Bland-Hawthorn, J., York, D. G., & Pimbblet, K. 2010 AJ, 139 794

Dekel, A. & Birnboim, Y. 2008, MNRAS, 383, 119

Dickey, J., & and Lockman, F. J. 1990, ARA&A, 28, 21

Dilday, B., et al. 2008, ApJ, 682, 262

Dilday, B., et al. 2010, ApJ, 715, 1021

Diehl, S. & Statler, T. S. 2007, ApJ, 668, 150

Diehl, S., & Statler, T. S. 2008, ApJ, 687, 986

Dunn, R. J. H., Allen, S. W., Taylor, G. B., Shurkin, K. F., Gentile, G., Fabian, A. C., & Reynolds, C. S. 2009, MNRAS, 404, 189

Faber, S. M., & Gallagher, J. S. 1976, ApJ, 204, 365

Faber, S. M., et al. 2007, ApJ, 665, 265

Ferrarese, L., et al. 2006, ApJ, 644, L21

Forbes, D. A., Proctor, R., Strader, J., Brodie, J. P. 2007, ApJ, 659, 188

Gibson, B. K., Loewenstein, M., & Mushotzky, R. F. 1997, MNRAS, 290, 623

Graves, G. J., Faber, S. M., Schiavon, R. P., & Yan, R. 2007, ApJ, 671, 243

Hayashi, K., Fukazawa, Y., Tozuka, M., Nishino, S., Matsushita, K., Takei, Y., & Arnaud, K. A. 2009, PASJ, 61, 1185

Henley, D. B., Shelton, R. L., Kwak, K., Joung, M. R., & Mac Low, M. 2010, ApJ, 723, 935

Ho, L. C., Greene, J. E., Filippenko, A. V., & Sargent, W. L. W. 2009, ApJ, 699, 626

Hopkins, P. F., Bundy, K., Hernquist, L., Wuyts, S., & Cox, T. J. 2010, MNRAS, 401, 1099

Hopkins, P. F., Hernquist, L., Cox, T. J., Keres, D., & Wuyts, S. 2009, ApJ, 691, 1424

Horiuchi, S., & Beacom, J. F. 2010, ApJ, 723, 329

Howell, J. H. 2005, AJ, 130, 2065

Humphrey, P. J., & Buote, D. A. 2006, ApJ, 639, 136

Humphrey, P. J., & Buote, D. A. 2008, ApJ, 689, 983

Humphrey, P. J.,Buote, D. A., Brighenti, F., Gebhardt, K., & Mathews, W. G. 2008, ApJ, 683, 161

Humphrey, P. J., Buote, D. A., Gastaldello, F., Zappacosta, L., Bullock, J. S., Brighenti, F., & Mathews, W. G. 2006, ApJ, 646, 899

Irwin, J. A., Athey, A. E., & Bregman, J. N. 2003, ApJ, 587, 356

Ishisaki, Y., et al. 2007, PASJ, 59, S113

Iwamoto, K,. Brachwitz, F., Nomoto, K., Kishimoto, N., Umeda, H., Hix, W. R., & Thielemann, F.-K. 1999, ApJS, 125, 439

Jackson, A. P., Calder, A. C., Townsley, D. M., Chamulak, D. A., Brown, E. F., & Timmes, F. X. 2010, ApJ, 720, 99

Jansen F., et al. 2001, A&A, 365, L1

Ji, J., Irwin, J. A., Athey, A., Bregman, J. N., & Lloyd-Davies, E. J. 2009 ApJ, 696, 2252 (Ji09)

Johansson, P. H., Naab, T., & Ostriker, J. P. 2009 ApJ, 697, L38

Kaviraj, S. 2010, MNRAS, 408, 170

Kaviraj, S., Khochfar, S., Schawinski, K., Yi, S. K., Gawiser, E., Silk, J., Virani, S. N., Cardamone, C. N., van Dokkum, P. G., & Urry, C. M. 2008, MNRAS, 388, 67

Kaviraj, S., Peirani, S., Khochfar, S., Silk, J., & Kay, S. 2009, MNRAS, 394, 1713

Keres, D., Katz, N., Fardal, M., Davé, R. & Weinberg, D. H. 2009, MNRAS, 395, 160

Kobayashi, C., Umeda, H., Nomoto, K., Tominaga, N., & Ohkubo, T. 2006, ApJ, 653, 1145

Komiyama, M., Sato, K., Nagino, R., Ohashi, T., & Matsushita, K. 2009, PASJ, 61, S337

Koyama, K., et al. 2007, PASJ, 59, S23

Krueger, B. K., Jackson, A. P., Townsley, D. M., Calder, A. C., Brown, E. F., & Timmes, F. X. 2010, ApJ, 719, L5

Kuntz, K. D., & Snowden, S. L. 2008, A&A, 478, 575

Kushino, A., Ishisaki, Y., Morita, U., Yamasaki, N. Y., Ishida, M., Ohashi, T., & Ueda, Y. 2002, PASJ, 54,327

La Barbera, F., Ferreras, I., de Carvalho, R. R., Lopes, P. A. A., Pasquali, A., de la Rosa, I. G., & De Lucia, G. 2011, ApJ, in press (arXiv:1108.0946)

Lei, S., Shelton, R. L., & Henley, D. B. 2009, 699, 1891

Li, W., Chornock, R., Leaman, J., Filippenko, A. V., Poznanski, D., Wang, X., Ganeshalingam, M., & Mannucci, F. 2011, MNRAS, 412, 1473

Loewenstein, M. & Davis, D. S. 2010, ApJ, 716, 384

Loewenstein, M., Valinia, A., & Mushotzky, R. F. 2001, ApJ, 547, 722

Lu, Y., Keres, D., Katz, N., Mo, H. J., Fardal, M., Weinberg, & M. D. 2011, MNRAS, 416, 660

Maeda, K., Ropke, F. K., Fink, M., Hillebrandt, W., Travaglio, C., & Thielemann, F.-K. 2010, ApJ, 712, 624

Mannucci, F., Cresci, G., Maiolino, R., Marconi, A., & Gnerucci, A. 2010, MNRAS, 408, 2115

Mannucci, F., Della Valle, M., & Panagia, N. 2006, MNRAS, 370, 773

Mannucci, F., Maoz, D., Sharon, K., Botticella, M. T., Della Valle, M., Gal-Yam, A., & Panagia, N. 2008, MNRAS, 383, 1121

Maoz, D., Mannucci, F., Li, W., Filippenko, A. V., Della Valle, M., & Panagia, N. 2011, MNRAS, 412, 1508

Maoz, D., Sharon, K., & Gal-Yam, A. 2010, ApJ, 722, 1879

Mathews W. G. 1989, AJ, 97, 42

Mathews, W. G. 1990, Astrophysics and Space Science Library, 160, 265

Mathews, W. G., & Brighenti, F. 2003, ARA&A, 41, 191

Mathews, W. G., Brighenti, F., & Buote, D. A. 2004, ApJ, 615, 662

Mathews, W. G., Brighenti, F., Faltenbacher, A., Buote, D. A., Humphrey, P. J., Gastaldello, F., & Zappacosta, L. 2006 ApJ, 652, L17

Matsushita, K., et al. 2007, PASJ, 59, S327

McNamara, B. R., & Nulsen, P. E. J. 2007, ARA&A, 45, 117

Mennekens, N., Vanbeveren, D., De Greve, J. P., & De Donder, E. 2010, A&A, 515, 89

Mitsuda, K. et al. 2007, PASJ, 59, S1

Molendi, S., De Luca, A, & Leccardi, A. 2004 A&A, 419, 837

Mulchaey, J. S., & Jeltema, T. E. 2010, ApJ, 715, L1

Murakami, H., Komiyama, M., Matsushita, K., Nagino, R., Sato, T., Sato, K., Kawaharada, M., Nakazawa, K., Ohashi, T., & Takei, Y. 2011, PASJ, in press

Naab, T., Johansson, P. H., & Ostriker, J. P. 2009, ApJ, 699, L178

Nagino, R., & Matsushita, K. 2009, A&A, 501, 157

Nagino, R., & Matsushita, K. 2010, PASJ, 62, 787

Nakajima, H., et al. 2008, PASJ, 60, S1

Nipoti, C., & Binney, J. 2007, MNRAS, 382 1481

Nomoto, K., Iwamoto, K., Nakasato, N., Thielemann, F.-K., Brachwitz, F., Tsujimoto, T., Kubo, Y., & Kishimoto, N. 1997, Nucl. Phys. A, 621, 467

Nulsen, P. E. J., Jones, C., Forman, W., Churazov, E., McNamara, B. R., David, L., & Murray, S. S. 2009, in "The Monster's Fiery Breath: Feedback in Galaxies, Groups, and Clusters", Eds. S. Heinz & E. Wilcots, AIP, p. 198

Pipino, A., Kawata, D., Gibson, B. K., & Matteucci, F. 2005, A&A, 434, 553

Pipino, A., & Matteucci, F. 2004, MNRAS, 347, 968

Pipino, A., & Matteucci, F. 2006, MNRAS, 365, 1114

Pipino, A., & Matteucci, F. 2008, A&A, 486, 763

Pipino, A., & Matteucci, F. 2011, A&A, 530, 98 (PM11)

Randall, S. W., Sarazin, C. L., & Irwin, J. A. 2004, ApJ, 600, 729

Randall, S. W., Sarazin, C. L., & Irwin, J. A. 2006, ApJ, 636, 200

Robaina, A. R., Bell, E. F., van der Wel, A., Somerville, R. S., Skelton, R. E., McIntosh, D. H., Meisenheimer, K., & Wolf, C. 2010, ApJ, 719, 844

Romano, D., Karakas, A. I., Tosi, M., & Matteucci, F. 2010, A&A, 522, 32

Ruiter, A. J., Belczynski, K., Fryer, C. 2009, ApJ, 699, 2026

Sanchez-Blazquez, P., Gibson, B. K., Kawata, D., Cardiel, N., & Balcells, M. 2009, MNRAS, 400, 1264

Sanchez-Blazquez, P., Gorgas, J., Cardiel, N., & Gonxalez, J. J. 2006, A&A, 457, 787

Sato, K., Matsushita, K., Ishisaki, Y., Yamasaki, N. Y., Ishida, M., & Ohashi, T. 2009, PASJ, 61, S353

Schawinski, K., Thomas, D., Sarzi, M., Maraston, C., Kaviraj, S., Joo, S.-J., Yi, S. K., & Silk, J. 2007, MNRAS, 382, 1415

Serlemitsos, P. J., et al. 2007, PASJ, 59, S9

Serra, P., & Oosterloo, T. A. 2010, MNRAS, 401 L29

Shankar, F., Marulli, F., Bernardi, M., Dai, X., Hyde, J. B., & Sheth, R. K. 2010, MNRAS, 403, 117

Shurkin, K., Dunn, R. J. H., Gentile, G., Taylor, G. B., & Allen, S. W. 2008, MNRAS, 383, 923

Smith, R. J., Lucey, J. R., Hudson, M. J., & Bridges, T. J. 2009, MNRAS, 398, 119

Snowden, S. L., Mushotzky, R. F., Kuntz, K. D., & Davis, D. S. 2008, A&A, 478, 615

Tang, S., & Wang, Q. D., MNRAS, 408, 1011

Tawa, N., et al. 2008, PASJ, 60, S11

Tawara, Y., Matsumoto, C., Tozuka, M., Fukazawa, Y., Matsushita, K. & Anabuki, N. 2008, PASJ, 59, S327

Thomas, D., Maraston, C., Bender, R., & de Oliveira, C. M. 2005, ApJ, 621, 673

Thomas, D., Maraston, C., Schawinski, K. Sarzi, M., & Silk, J. 2010, MNRAS, 404, 1775

Tonry, J. L., Dressler, A., Blakeslee, J. P., Ajhar, E. A., Fletcher, A. B., Luppino, G. A., Metzger, M. R., & Moore, C. B. 2001, ApJ, 546, 681

Tozuka, M., & Fukazawa, Y. 2008, PASJ, 60, 527

Trager, S. C., Faber, S. M., Worthey, G., & Gonzlez, J. J. 2000, AJ, 119, 1645

Trager, S. C., Faber, S. M., Worthey, G., & Gonzlez, J. J. 2000, AJ, 120, 165

Uchiyama, H., et al. 2009, PASJ, 61, 9

van der Wel, A. Bell, E. F., van den Bosch, F. C., Gallazzi, A., & Rix, H.-W. 2009 ApJ, 698, 1232

Tal, T., van Dokkum, P. G., Nelan, J. & Bezanson, R. 2009, AJ, 138, 141

Trujillo, I., Ferreras, I., & de La Rosa, I. G. 2011, MNRAS, 415, 3903

van de Voort, F., Schaye, J., Booth, C. M., & Dalla Vecchia, C. 2011, MNRAS, 414, 2458

van Dokkum, P. G., Franx, M., Kriek, M., Holden, B., Illingworth, G. D., Magee, D., Bouwens, R., Marchesini, D., Quadri, R., Rudnick, G., Taylor, E. N., & Toft, S. 2008, ApJ, 677, L5

Vega, O., Bressan, A., Panuzzo, P., Rampazzo, R., Clemens, M., Granato, G. L., Buson, L., Silva, L., & Zeilinger, W. W. 2010, ApJ, 721, 1090

Wilms, J., Allen, A., & McCray, R. 2000, ApJ, 542, 941

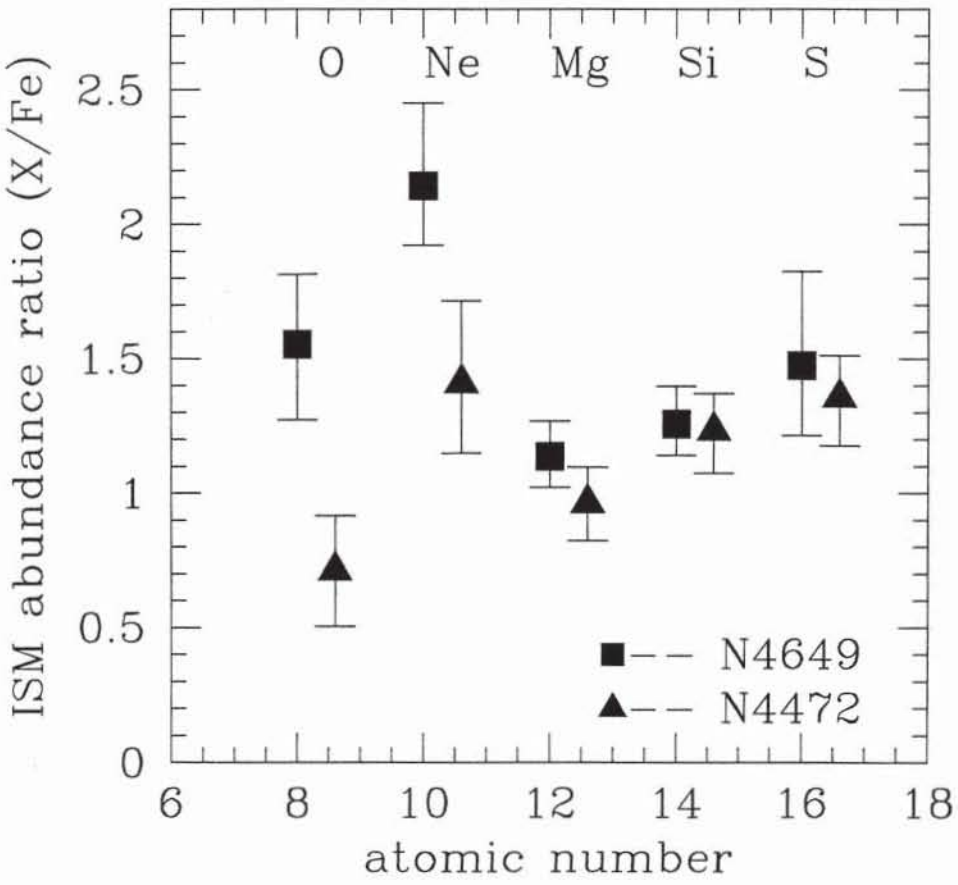

Fig. 7.— Abundance pattern comparison between NGC 4649 (solid squares) and NGC 4472 (solid triangles). The NGC 4472 values from Paper I have been rescaled to the Asplund et al. (2009) solar standard.

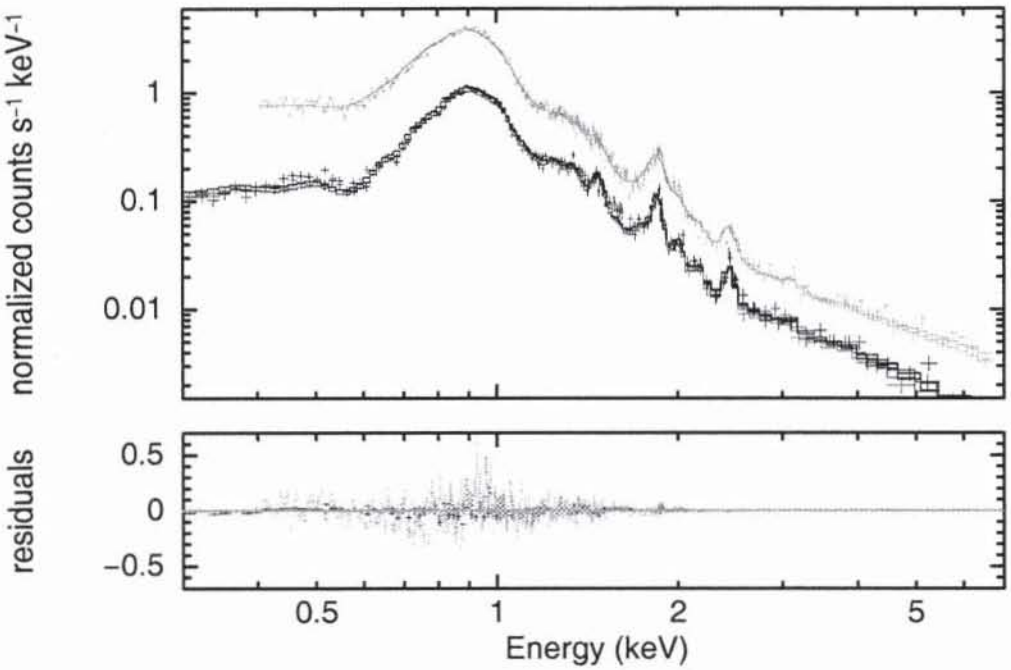

Fig. 8.— 0 – 2′ 2001 *XMM-Newton* EPIC spectra (MOS1: black, MOS2: red, PN: green) and best-fit model with residuals (Table 5). The spectra are fit over the 0.3-5.5 keV band for the MOS and the 0.4-5.5 keV band for the PN.

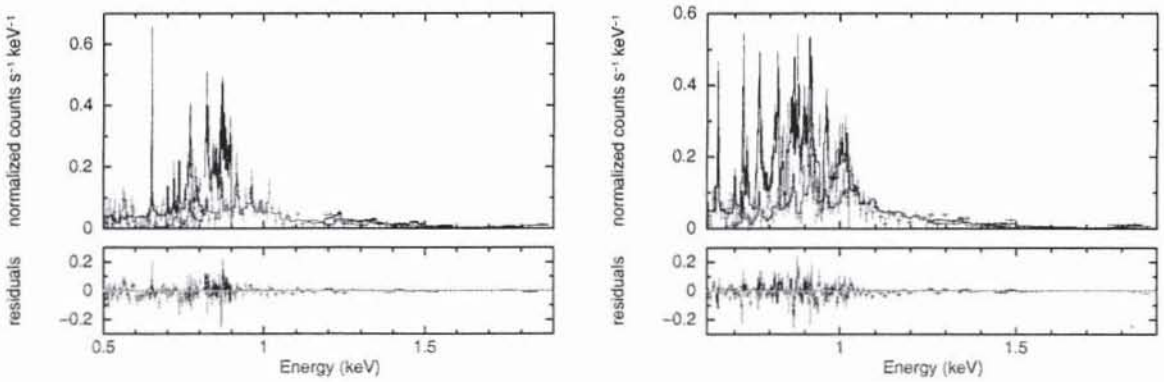

Fig. 9.— RGS spectra (2007 Observation) and best-fit **vapec** thermal plasma model (Table 5), and residuals. RGS-1 (*left* panel, (a)) and RGS-2 (*right* panel, (b)) are broken out for clarity. First and second order spectra, included in the fitting, are shown.

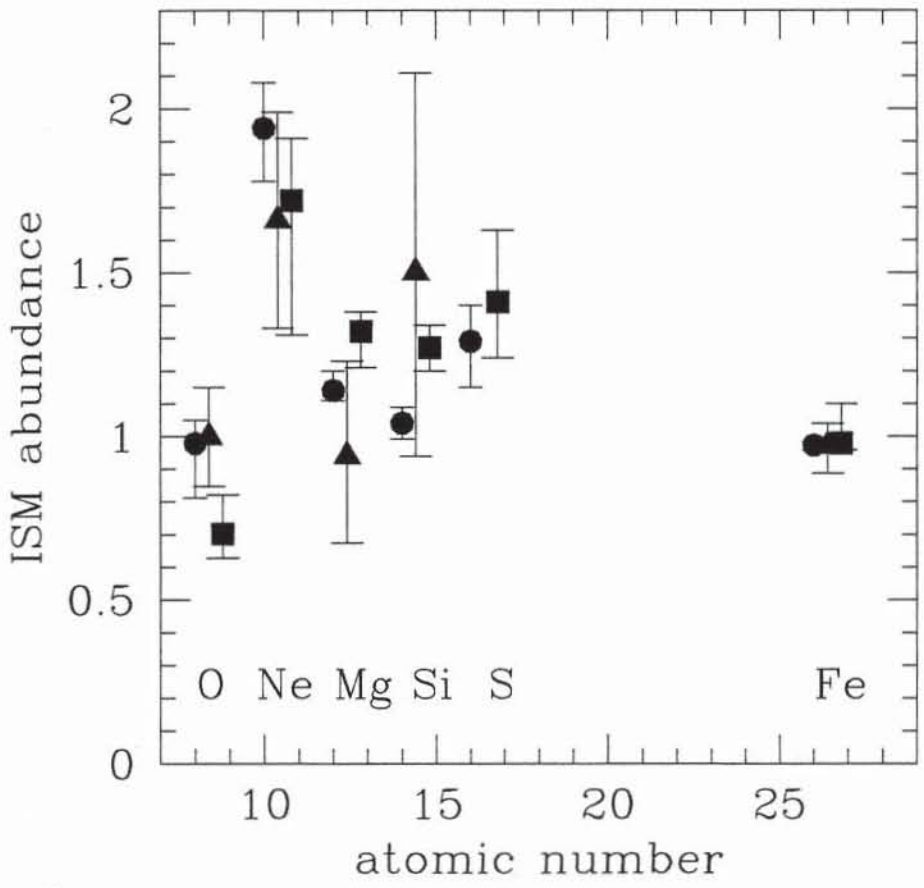

Fig. 10.— Abundance pattern comparison for separate fits to *XMM-Newton* EPIC $0-2'$ (solid squares) and RGS (solid triangles) and *Suzaku* XIS $0-2'$ (solid circles) spectra.

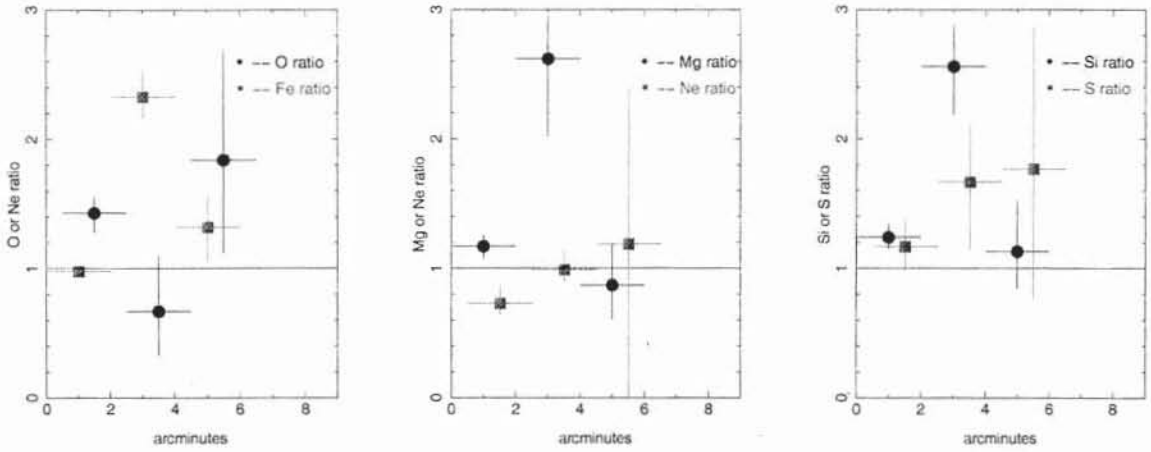

Fig. 11.— Ratio of the abundances derived from the *XMM-Newton* EPIC data to those of the *Suzaku* XIS detectors. We show Fe and O (*left* panel, (a)), Si and S (*middle* panel, (b)), Mg and Ne (*right* panel, (c)) ratio profiles. The points represented by circles are shifted to the right by 0.5′.

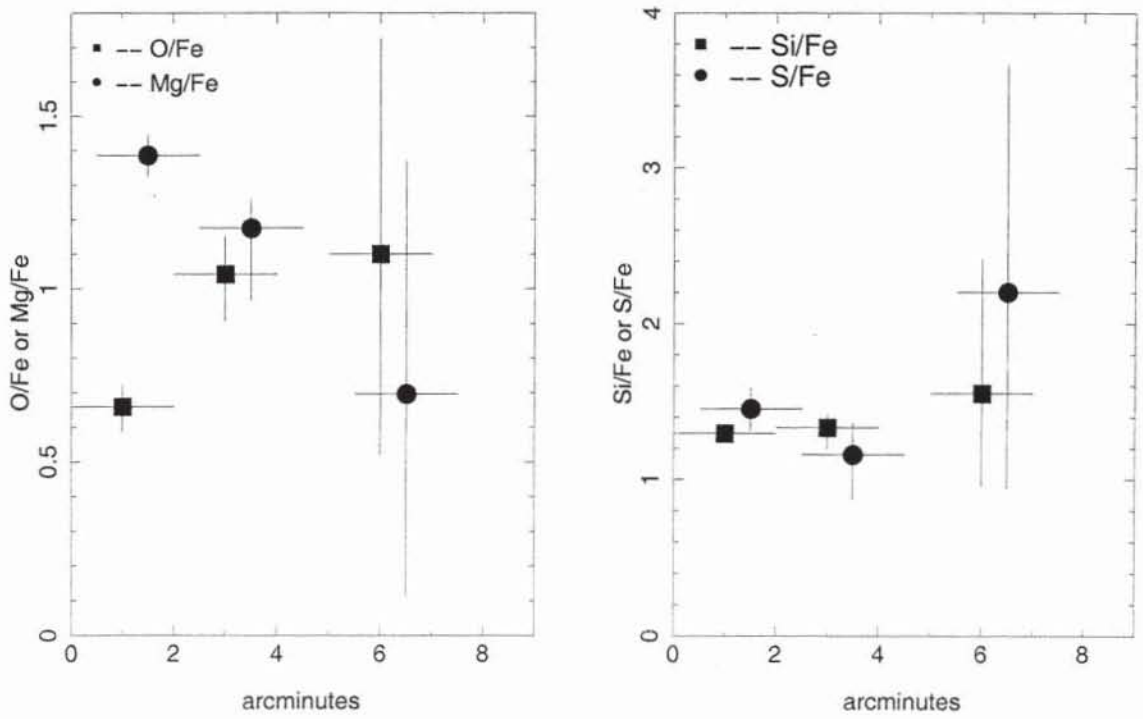

Fig. 12.— Profiles of abundance ratios with respect to Fe for O and Mg (*left* panel, (a)); and, Si and S (*right* panel, (b)) derived from the EPIC data.

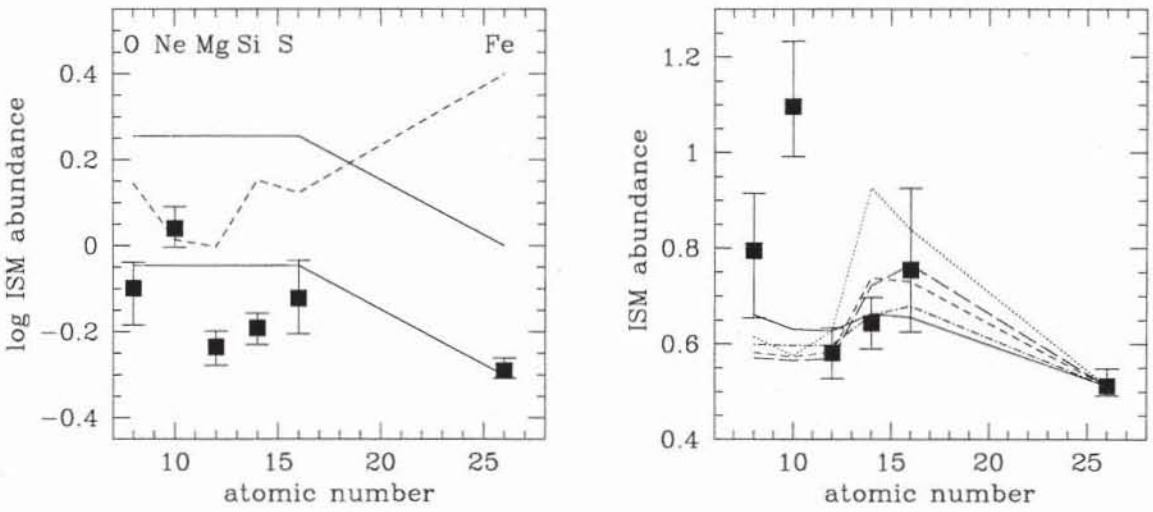

Fig. 13.— *Left* panel (a): Comparison of NGC 4649 abundance pattern (filled squares) and three simple model predictions: stars-only enrichment with $[Fe/H]_{\rm stars} = 0$ and -0.3 (upper and lower solid lines), and the best-fit model with $[Fe/H]_{\rm stars} = -0.3$ and SNIa exploding at the standard rate (C-DEF yields, broken line). *Right* panel (b): Best-fit solutions to equation (4) to the NGC 4649 abundance ratio pattern (excluding Ne) for the following SNIa abundance sets: Maeda et al. (2010) C-DEF, C-DDT, and O-DDT models (solid, dotted, and short-dashed lines), Iwamoto et al. (1999) WDD1 and WDD3 (long-dashed, dot-dashed lines; the WDD2 solution closely resembles that for the O-DDT yields). The solutions, which predict only relative abundances, are scaled to the observed ISM Fe abundance.

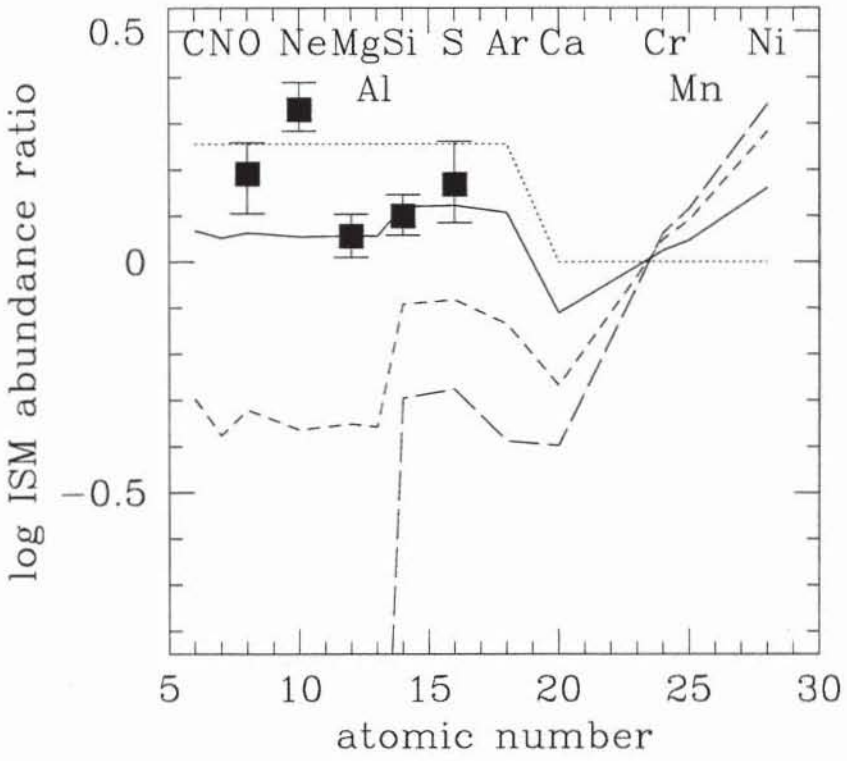

Fig. 14.— Best-fit model to the observed abundance pattern derived from *Suzaku* data (filled squares) assuming equal numbers of C-DEF, O-DDT, and WDD3 SNIa (solid line), compared with the ratios for pure stellar (dotted) and SNIa (long-dashed) enrichment and that for $\theta_{\rm SNIa} = 1$, $r_{\rm in}\phi_{\rm in} = 0$ (standard SNIa rate, no inflow; short-dashed line).

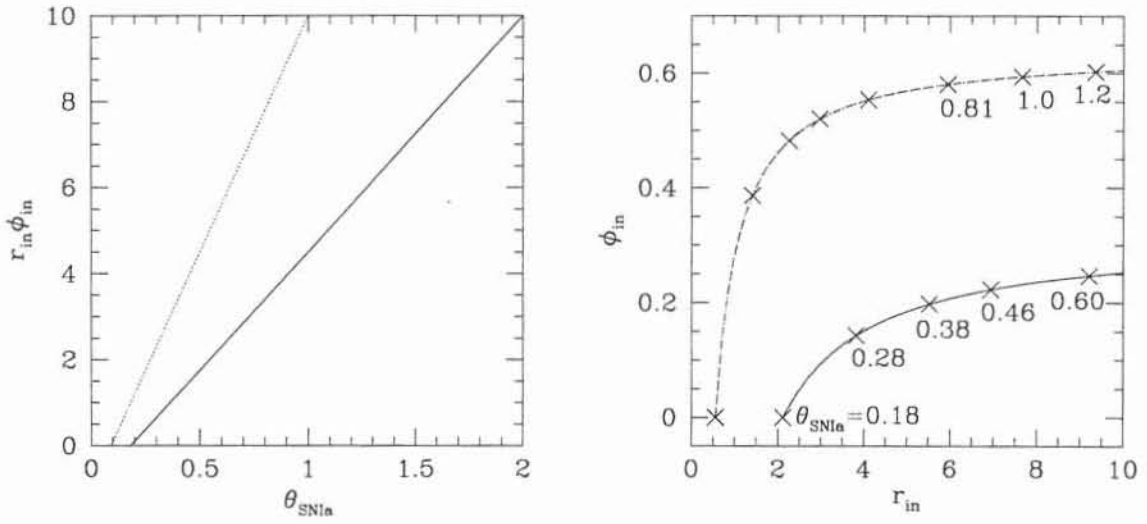

Fig. 15.— *Left* panel (a): $r_{\rm in}\phi_{\rm in}$ vs. $\theta_{\rm SNIa}$ for the best-fit model (solid line in Figure 14). Also shown, is the corresponding curve for $[Fe/H]_{\rm stars} = -0.3$ (dotted line). *Right* panel (b): $\phi_{\rm in}$ vs. $r_{\rm in}$ implied by the observed $f_{\rm ISM}^{\rm Fe}$ for the best-fit abundance ratio patterns assuming $[Fe/H]_{\rm stars} = 0$ and $b_{\rm out} = 0.0$ (solid curve) or 1.0 (broken curve). The corresponding $\theta_{\rm SNIa}$ are shown by crosses; the first five values are the same for each curve. *Abundance ratios* are invariant along the lines in (a); *abundances* are invariant along the curves in (b) for the specified SNIa rates.

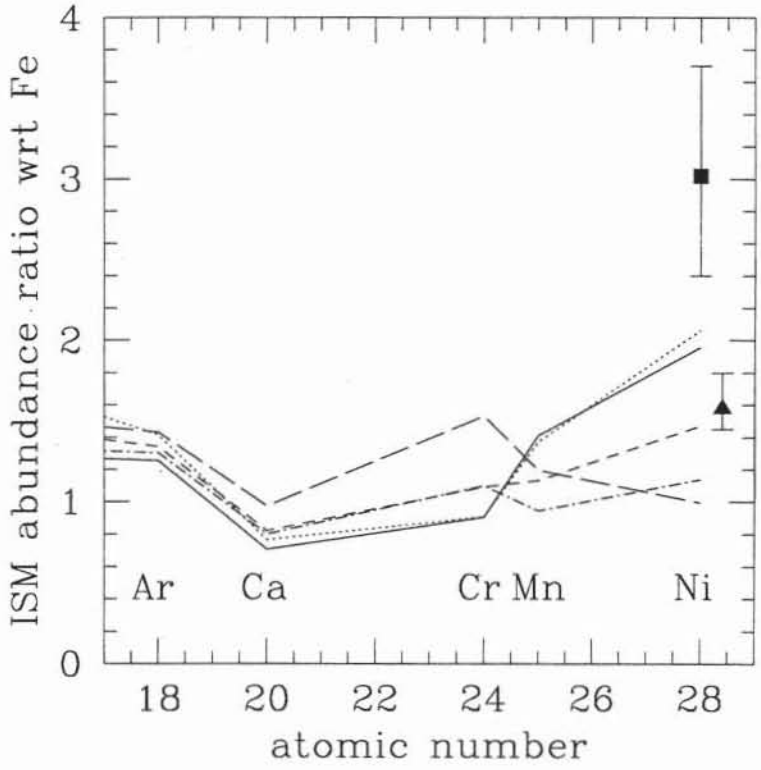

Fig. 16.— Same as Figure 13b, focusing on the Fe group elements, with Ni/Fe abundance ratios from RGS (solid square) and XIS $0-2'$ (solid triangle) spectral fits.

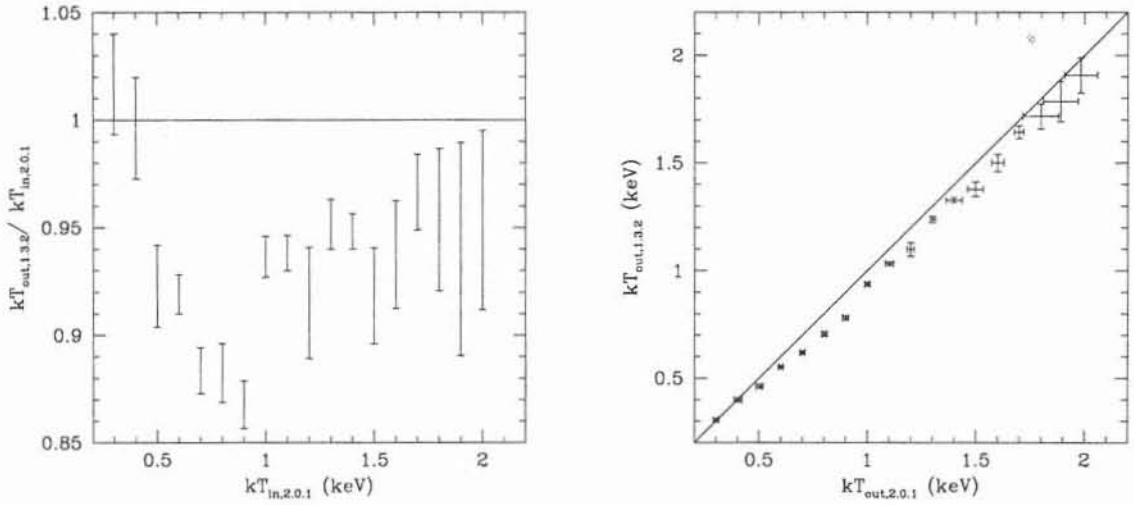

Fig. 17.— *Left* panel (a): Ratio of the best-fit temperature using *AtomDB* v1.3.2, to the *AtomDB* v2.0.1 simulation input temperature, versus simulation input temperature. *Right* panel (b): Best-fit temperature using *AtomDB* v1.3.2. versus best-fit temperature using *AtomDB* v2.0.1.

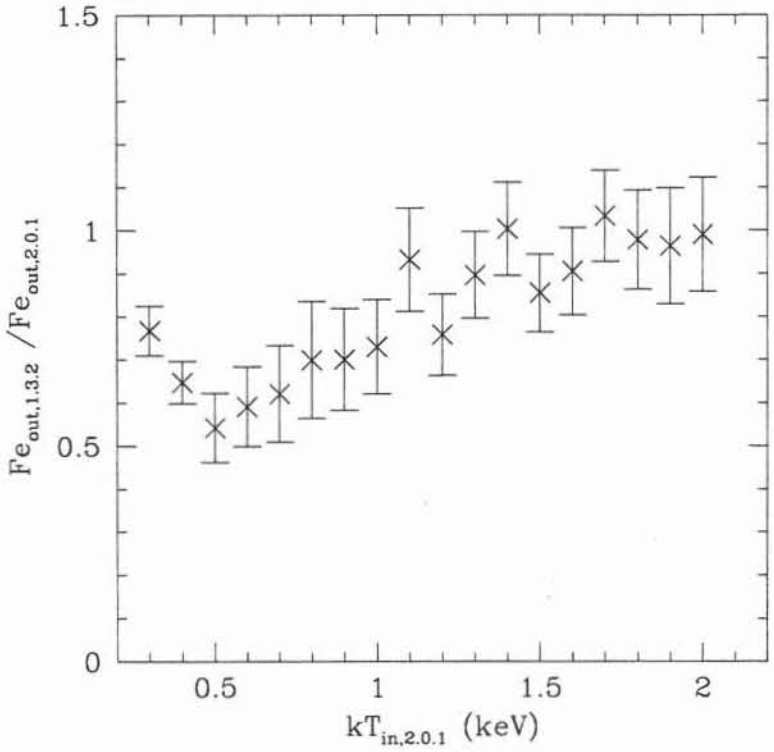

Fig. 18.— Ratio of the best-fit Fe abundance using *AtomDB* v1.3.2, to the best-fit that using *AtomDB* v2.0.1, versus simulation input temperature.

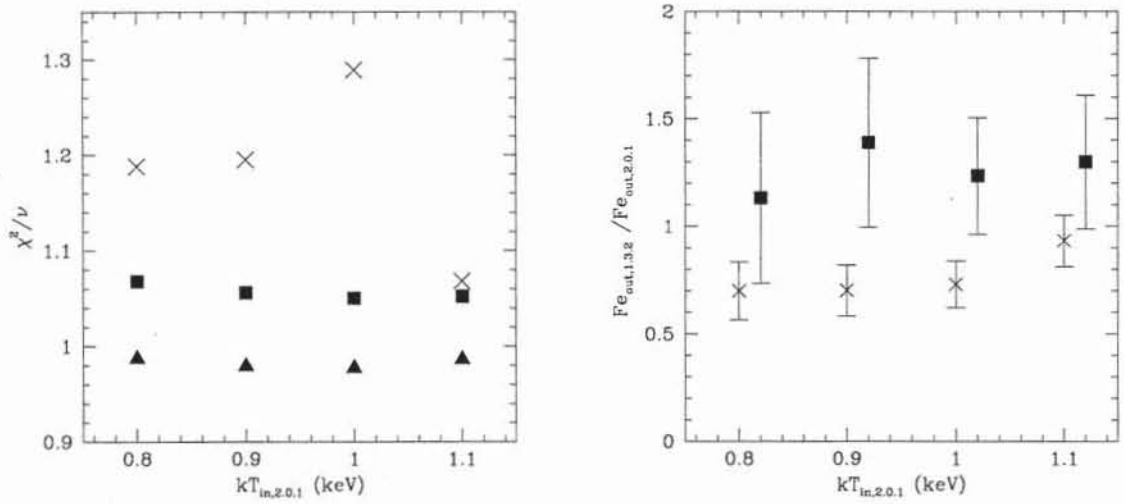

Fig. 19.— *Left* panel (a): Reduced-χ^2 values for fits to simulated *AtomDB* v2.0.1 spectra with $kT_{in,2.0.1}$ for fits using (the "correct") *AtomDB* v2.0.1 single-temperature models (filled triangles), *AtomDB* v1.3.2 single-temperature models (crosses), and *AtomDB* v1.3.2 two-temperature models (filled squares). *Right* panel (b): Same as Figure 19a for the Fe abundance, showing single- (crosses) and two-temperature (filled squares) models.